Geometrically frustrated systems

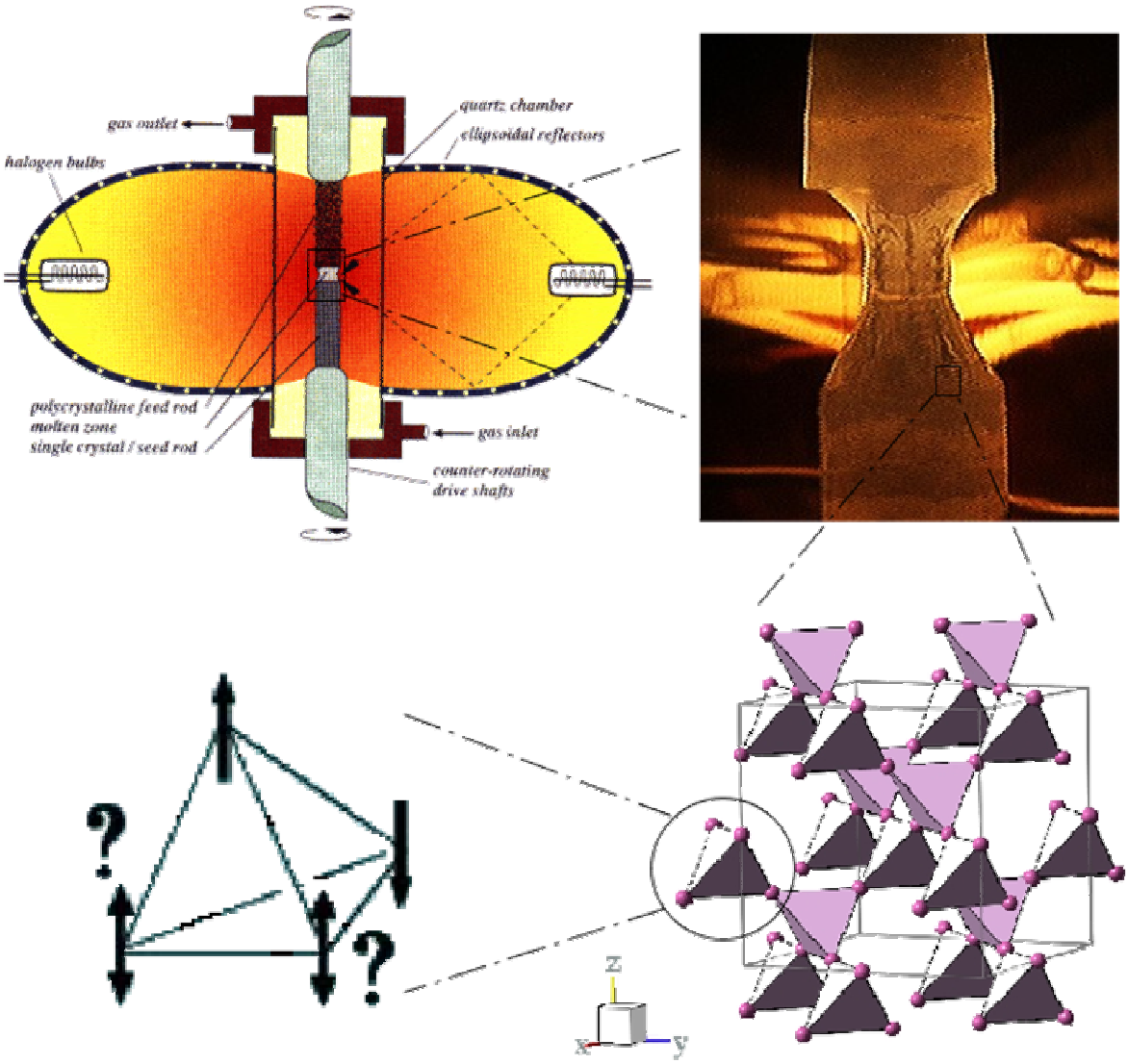

Tom Lummen, Optical Condensed Matter Physics, Rijks*universiteit* Groningen, sept. 2004-juli 2005

Contents **Page**

- A.) Introduction 3-11
  - A.1.) The phenomenon of geometrical frustration 3-4
  - A.2.) Geometrical frustration in the systems studied in this work 4-10
    - A.2.1) Frustration in the pyrochlore lattice 4-9
      - A.2.1.I) Spin liquid 4-5
      - A.2.1.II) Partial ordering 5-6
      - A.2.1.III) Spin ice 6-8
      - A.2.1.IV) Spin glass 8
      - A.2.1.V) The 'spin-Teller' effect 8-9
    - A.2.2.) Frustration in the triangular lattice 9-10
  - A.3.) Motivation for this work 11

- B.) Single crystal growth using the floating zone technique 12-25
  - B.1.) Growth of terbium titanate ($Tb_2Ti_2O_7$) single crystals 13-15
    - B.1.1.) Crystal $Tb_2Ti_2O_7$-A 14
    - B.1.2.) Crystal $Tb_2Ti_2O_7$-B 14-15
    - B.1.3.) Crystal $Tb_2Ti_2O_7$-C 15
    - B.1.4.) Crystal $Tb_2Ti_2O_7$-D 15
  - B.2.) Growth of gadolium titanate ($Gd_2Ti_2O_7$) single crystals 16
    - B.2.1.) Crystal $Gd_2Ti_2O_7$-A 16
    - B.2.2.) Crystal $Gd_2Ti_2O_7$-B 16
  - B.3.) Growth of holmium titanate ($Ho_2Ti_2O_7$) single crystals 17
    - B.3.1.) Crystal $Ho_2Ti_2O_7$-A 17
    - B.3.2.) Crystal $Ho_2Ti_2O_7$-B 17
  - B.4.) Growth of dysprosium titanate ($Dy_2Ti_2O_7$) single crystals 18-19
    - B.4.1.) Crystal $Dy_2Ti_2O_7$-A 18
    - B.4.2.) Crystal $Dy_2Ti_2O_7$-B 18-19
  - B.5.) Growth of a cuprous ferrite ($CuFeO_2$) single crystal 19-22
    - B.5.1.) Crystal $CuFeO_2$-A 21-22
    - B.5.2.) Crystal $CuFeO_2$-B 22
  - B.6.) Further growth attempts 22-25
    - B.6.1) Attempted growth of a zinc chromite ($ZnCr_2O_4$) crystal 23-24
    - B.6.2) Attempted growth of an yttrium molybdate ($Y_2Mo_2O_7$) crystal 24-25

- C.) Results & Discussion 26-44
  - C.1.) Magnetic susceptibility measurements 26-31
    - C.1.1.) Magnetic susceptibility of terbium titanate ($Tb_2Ti_2O_7$) 26-27
    - C.1.2.) Magnetic susceptibility of gadolium titanate ($Gd_2Ti_2O_7$) 27-28
    - C.1.3.) Magnetic susceptibility of holmium titanate ($Ho_2Ti_2O_7$) 28-29
    - C.1.4.) Magnetic susceptibility of holmium titanate ($Ho_2Ti_2O_7$) 29-31
  - C.2.) Preparation of Raman samples: X-ray Laue diffraction and sample polishing 31-33
  - C.3.) Raman spectroscopy 33-44
    - C.3.1.) Raman spectroscopy of terbium titanate ($Tb_2Ti_2O_7$) 33-40
    - C.3.2.) Raman spectroscopy of gadolinium titanate ($Gd_2Ti_2O_7$) 41-44

- D.) Conclusions & Future prospects 45

- E.) Aknowledgements 46

A.) Introduction

A.1.) The phenomenon of geometrical frustration

There are many interesting systems in nature which exhibit the phenomenon of 'geometrical frustration'.[1,2] This term applies to a system, when it is not able to simultaneously satisfy all of its magnetic exchange interactions, solely due to its geometry. The simplest example of this phenomenon is the case of 3 equal, antiferromagnetically interacting Ising spins residing on the corners of a triangle of equal sides (fig. 1.).

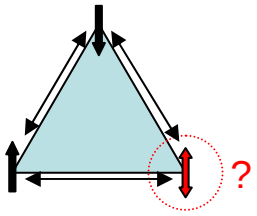

Fig. 1: *3 antiferromagnetically coupled Ising spins on a triangle are 'frustrated'.*

In this case, no matter how the spins are configured, there is always one unfavourable interaction between a pair of neighbouring spins, since they are ferromagnetically aligned with respect to each other. Note that this is completely due to the geometry of the system. There are several different lattices occurring in nature which provide a geometry suitable to induce such frustration. The most famous ones being the 2D triangular lattice (Fig. 2.a.), the 2D Kagomé lattice (Fig. 2.b.) of corner-sharing triangles and the 3D pyrochlore lattice of corner-sharing tetrahedra (Fig.2. c.). If a magnetic species resides on any of these lattices, frustration may occur.

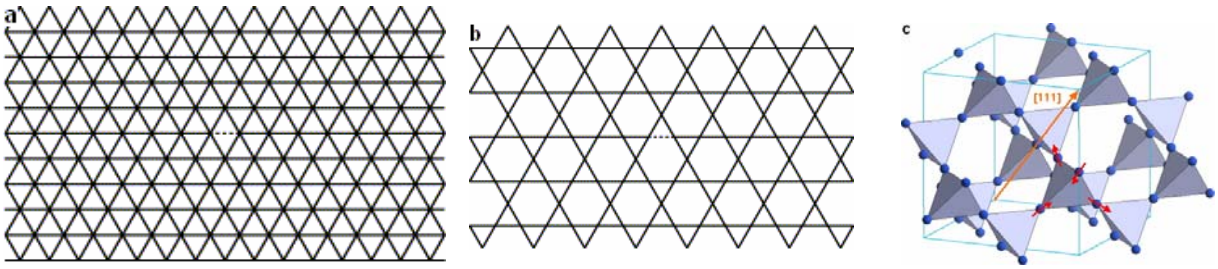

Fig. 2*: Schematic drawings of lattice geometries suitable to induce magnetic frustration.* ***a.*** *(left) 2D triangular lattice* ***b****. (middle) 2D Kagomé lattice* ***c.*** *(right) 3D pyrochlore lattice. In both scheme a and b, atoms reside on the intersections of the lines, while in drawing c, the atoms are on the corners of the tetrahedra, indicated by the small, blue spheres.*

Although there is no possible way in which a geometrically frustrated system can satisfy all of its interactions simultaneously, there are many possibilities for it to minimize the maximum number of interactions. If one considers the simplest example of fig. 1, there are already 6 different arrangements of the spins that lead to the same interaction energy. Expanding this picture to extended lattices, one can easily imagine that geometrically frustrated systems typically have a very large number of states which have the same, lowest possible energy. In other words, a frustrated system has a macroscopically degenerate magnetic ground state. As a result of this magnetic ground state degeneracy, frustrated systems usually do not exhibit long-range magnetic order down to very low (mK-range) temperatures, at an energy scale much lower than the energy scale of their exchange interactions. At these very low temperatures even the smallest perturbation in the system's corresponding Hamiltonian (any perturbation that leads to an energy difference of the order of mK, for instance single-ion or exchange anisotropy, dipolar interactions, further neighbour interactions, a magnetic field or small lattice distortions) can favour certain magnetic ground states above others and thus (partially) lift this degeneracy. This also accounts for the vast richness and diversity of the low temperature magnetic behaviour of different frustrated systems in nature. The implication that the pyrochlore antiferromagnet might have non-zero entropy (multiple ground states) even at T = 0 K is of course quite fascinating. The fact that magnetic fluctuations would

persist even down to absolute zero temperature shows these frustrated systems do not obey the third law of thermodynamics, which states that the entropy of a pure, perfectly crystalline substance at absolute zero is 0.

A.2.) Geometrical frustration in the systems studied in this work

As mentioned in the previous section, there are several lattices in nature, which provide a suitable geometry for frustration. This section describes in more detail the specific lattices of the systems studied in this work, their magnetic elements and their behaviour at low temperatures. The compounds investigated in this work can be divided into two groups in two different ways. In the different paragraphs of this section, they are separated on the basis of their magnetic lattices. The other way to divide the compounds into two groups is on the basis of the origin of their magnetism. First there is the $R_2Ti_2O_7$-family, wherein the magnetic species (the rare earth elements R = Tb, Gd, Ho, Dy) derive their magnetism from *4f* electrons. This family belongs to the pyrochlore group and is described in sections A.2.1.I) through A.2.1.III). In the second group of compounds, with the materials $Y_2Mo_2O_7$, $ZnCr_2O_4$ and $CuFeO_2$, the magnetism is derived from *3d*/*4d* electrons. $Y_2Mo_2O_7$ and $ZnCr_2O_4$ are both also based on the pyrochlore lattice and they are described in sections A.2.1.IV) and A.2.1.V), respectively, while $CuFeO_2$ has a triangular lattice and is thus addressed in section A.2.2.I). Since the *4f* orbitals are relatively small and close to the ion core, while the *3d*/*4d* orbitals are much more extended in space, the interactions in the compounds belonging to the '*3d*/*4d*-group' are much stronger and consequently, also the energy scale involved is much higher. The important aspects of all the compounds are summarized in table 1, at the end of this section.

A.2.1.) Frustration in the pyrochlore lattice

Most of the compounds studied have a magnetic pyrochlore lattice. In the class of $A_2B_2O_7$-compounds, both the A^{3+} ion, which can be any rare earth element and is coordinated to 8 oxygen atoms, and the B^{4+} ion, which can be any transition metal element and has a six-fold oxygen coordination, reside on a pyrochlore lattice. The compounds investigated here that belong to this class are the family of rare earth titanates, $R_2Ti_2O_7$, of which the R = Tb, Gd, Dy and Ho members are studied here, and the compound $Y_2Mo_2O_7$. In the rare earth titanate family, the rare earth element R^{3+} the only magnetic species in the compound (Ti is in the 4+ valence state and is thus diamagnetic ($3d^0$), O^{2-} is also diamagnetic (filled shell: $2s^2 2p^6$)), the magnetic structure can be seen as a purely pyrochlore lattice (fig. 2.c.). The magnetic behaviour of the different members of this $R_2Ti_2O_7$-family at low temperatures is quite diverse. In $Y_2Mo_2O_7$ the only paramagnetic species is Mo^{4+} (Y^{3+} has an empty d shell ($4d^0$)). This is a very different case however, since here only the B^{4+} ion is paramagnetic, which has different coordination and magnetic nature (arising from *d*-electrons instead of *f*-electrons). Because the Mo^{4+} ion also resides on a pyrochlore lattice however, the same magnetic structure as constructed in the rare earth elements in $R_2Ti_2O_7$ is formed. In the spinel lattice, general formula AB_2O_4, the B^{3+} species reside on a pyrochlore lattice, meaning that in $ZnCr_2O_4$, where the only paramagnetic species is Cr^{3+} (Zn^{2+} ($3d^{10}$) is diamagnetic, as is O^{2-}), again the same pyrochlore magnetic structure is formed. Also in this case the magnetism arises from *d*-electrons.

A.2.1.I) Spin liquid

For the pyrochlore lattice, both theoretical considerations[3,4,5] and Monte Carlo simulations[5,6] predict a 'collective paramagnetic' ground state, meaning no long range magnetic ordering for classical Heisenberg (isotropic) magnetic interactions at finite temperature. The quantum Heisenberg spin (S = ½) model for the pyrochlore lattice also

shows a 'spin liquid' state as the ground state at finite temperature[7]. The terms 'collective paramagnet' (for the classical models) and 'spin liquid' (for the quantum models) are assigned to these ground states to point out that there are quite strong and non-trivial short-range (of the order of interactomic distances) spin correlations in the system, even though the system does not show long range magnetic order down to T = 0 K. These short-range spin correlations are analogous to the short-range position correlations in ordinary liquids, hence the name 'spin liquid'. In $Tb_2Ti_2O_7$, the Tb^{3+} ion (configuration $4f^8$) has a $^7F_6$ ground state and thus a spin S = 3. The experimentally extrapolated Curie-Weiss temperature for $Tb_2Ti_2O_7$, $\Theta_{C.W.} \approx -19$ K, indicates that the nearest-neighbour interactions between Tb^{3+} moments are antiferromagnetic[8]. Despite the energy scale of these interactions, the Tb^{3+} moments do not show long range magnetic order down to at least 50 mK[9], making it the 'cleanest' experimental example of a spin liquid in a 3D system to date. The fact that a system does not undergo a magnetic transition down to temperatures well below the measured value of $|\Theta_{C.W.}|$, is a typical characteristic of magnetically frustrated systems. Crystal field calculations indicate an Ising-like easy axis anisotropy for the Tb^{3+} magnetic moments along their local [111] directions (meaning the moments are restricted to pointing parallel or anti-parallel to the direction from the Tb-ion to the center of their tetrahedra), which would dramatically reduce the degree of frustration in this antiferromagnetic compound[10]. Neutron scattering results can, however, not be explained using a local [111] Ising dipolar model, whereas an anisotropic Heisenberg model does yield good agreement[11]. Which model is most appropriate to $Tb_2Ti_2O_7$ is currently still under discussion, and the mechanism responsible for the absence of magnetic order down to 70 mK remains unresolved at the moment[12].

A.2.1.II) Partial ordering

The Gd^{3+}-ion in $Gd_2Ti_2O_7$ has, in contrast to the Tb^{3+}-ion in Tb_2TiO_7, a spin only $^8S_{7/2}$ ground state. Thus, crystal field levels and possible induced Ising-like anisotropy are not expected to be significant in this member of the rare earth pyrochlore family. Its Curie-Weiss temperature has experimentally been determined to be $\Theta_{C.W.} \approx -9.6$ K[13], while it does not show magnetic ordering until a temperature of ~ 1 K (as state above, this is a general feature for frustrated magnets). The system undergoes a magnetic transition at $T_N \approx 1$ K, which was confirmed by magnetic susceptibility and specific heat measurements[14]. The entropy removal below this transition is however only about 50 %, indicating the system is not yet fully ordered below T_N. Powder neutron scattering data confirmed that this transition is a transition into an only partially ordered state, where only three spins per tetrahedron order. The fourth remains disordered down to 50 mK. This partiallly ordered state was described as a '1-*k* structure' (fig. 3.a); a set of 'q=0 ordered' 2D [111] Kagomé planes, separated by fluctuating magnetic moments at the interstitial sites, so-called 'multi-*k*' structures[15] could, however, not be excluded on the basis of that work. A subsequent specific heat study[16], as well as another neutron investigation showed a second transition at $T' \approx 0.7$ K, while also a vanishing ground state entropy was reported[17]. Based on these results, the second transition was ascribed to further, partial ordering of the fourth, disordered spin. The second neutron investigation also provided strong evidence that the magnetic structure below T' is a '4-*k*' structure (fig. 3.b), while between the two transitions, the structure is the previously ascribed '1-*k*' structure. Theoretically, since $Gd_2Ti_2O_7$ does not have significant Ising-like anisotropy, it should be a very good approximation to the Heisenberg antiferromagnet with strong dipolar couplings[14,18]. Experiments, however, have shown that equivalent sites are divided into ordered and disordered states, which is very rare among Heisenberg models[19]. Clearly, it has proven difficult to theoretically explain the experimentally determined magnetic structure and, as in the $Tb_2Ti_2O_7$ case, the search for the appropriate model to justify the low temperature magnetic behaviour is still ongoing.

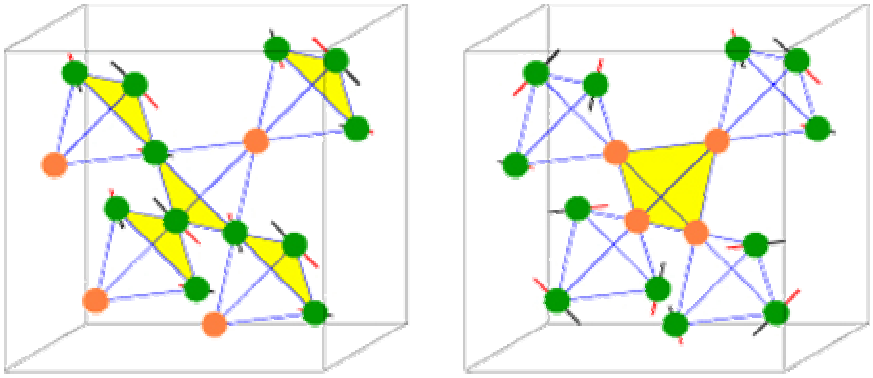

Fig. 3: *Schematic drawings of the '1-k'(left) and the '4-k' structure described in the text above. The ordered spins are on the green colored Gd^{3+}-ions, the orange Gd^{3+}-ions have (partially) disordered spins. In the 1-k structure, the ordered spins are perpendicular to a single, global crystallographic [111] direction, in a '120°-configuration', while in the 4-k structure, they are perpendicular to their local [111] axes (the direction of single-ion anisotropy in $Tb_2Ti_2O_7$). (taken from ref. 13)*

A.2.1.III) Spin ice

In both $Ho_2Ti_2O_7$ and $Dy_2Ti_2O_7$, the situation is quite different. The rare earth ions in these compounds have a ${}^5I_8$ (Ho^{3+}) and a ${}^6H_{15/2}$ (Dy^{3+}) ground state, respectively, with corresponding magnetic moments $\mu = 10.6\ \mu_B$ (Ho^{3+}) and $\mu = 9.7\ \mu_B$ (Dy^{3+}). These systems are well described by an Ising doublet, and were first thought to have weak *ferro*magnetic nearest neighbour exchange couplings with a strong Ising anisotropy along the local [111] axis of the spins[20,21]. The fact that the exchange interactions were ferromagnetic would, unlike for antiferromagnetically interacting spins with local [111] Ising anisotropy (as stated above), frustrate the lattice of corner sharing tetrahedra[20,22]. The ground state configuration of such systems would be such that every tetrahedron has both two spins pointing in and two spins pointing out of the tetrahedron, along their local [111] axis (fig. 4.). This nearest neighbour local [111] Ising ferromagnetic model turns out to map onto the *global* nearest neighbour Ising antiferromagnetic model on the same lattice of corner sharing tetrahedra[23]. The analogy of the latter model with Pauling's ice water model[24] was already pointed out by Anderson[25], about half a century ago. In Pauling's model for the 'hexagonal' ice phase, the oxygen atoms of H_2O are arranged on a lattice which can be visualized by putting the O atoms at the centers of the tetrahedra in the corner sharing tetrahedra structure. The hydrogen atoms are located on the O-O vectors, however since they are covalently bonded to only one O-atom, they are closer to one of the two. Since the ice consists of a network of hydrogen bonded H_2O molecules, ice is formed when the system is arranged according to the so-called 'ice rules':

I.) Exactly one hydrogen atom is located on each bond connecting two nearest neighbour oxygen atoms.

II.) Of the four hydrogen atoms surrounding each oxygen atom, exactly two are covalently bonded to this O-atom and thus 'close', while the other two are covalently bonded to other O-atoms and thus 'far'.

As can be seen in fig. 5., these 'ice rules' are equivalent to the ground state requirement of the nearest neighbour local [111] Ising ferromagnetic model, which was: two spins pointing into (corresponds to a 'close' hydrogen atom) and two spins pointing out of the tetrahedron ('far' hydrogen atom). These equivalent (under)constraints on analogous systems result in

both cases in the fact that there is not a single, unique ground state, but that there is a macroscopically large number of degenerate states of lowest energy. As stated above, if the degeneracy is not lifted by other perturbations in the corresponding Hamiltonian, it would lead to a finite zero-point entropy (residual entropy at T = 0 K). Because of the analogy between the two systems, lattices which display nearest neighbour local [111] Ising ferromagnetic interactions, such as $Ho_2Ti_2O_7$ and $Dy_2Ti_2O_7$, were named 'spin ice'[20,22,26].

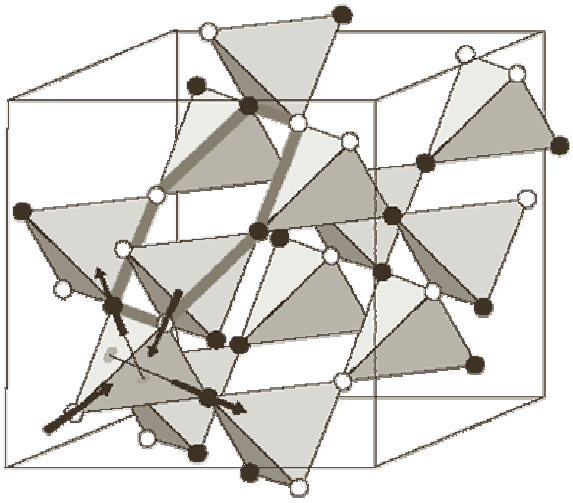

Fig. 4.: *The ground state configuration of the ferromagnetic local [111] anisotropy model. The white spheres correspond to spins pointing into a 'downward' tetrahedron, while black spheres correspond to spins pointing into an upwards pointing tetrahedron. The configuration for the spins is explicitly drawn for a downwards pointing tetrahedron. (taken from Gingras, M.J.P & den Hertog, B.C. Can. J. Phys.* ***79****, 1339 (2001))*

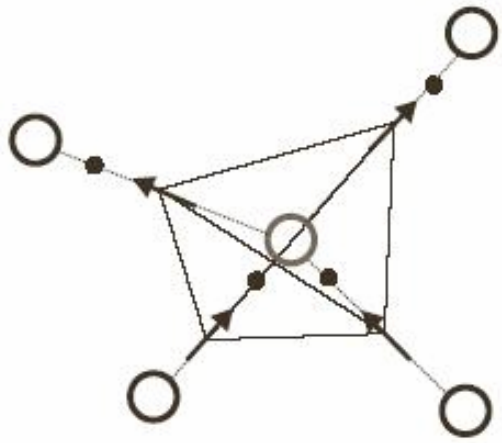

Fig. 5.: *The 'ice rules' and the ground state requirement of the nearest neighbour local [111] Ising ferromagnetic (NNLIF) model depicted in one drawing. Large circles (oxygen atoms) and small black spheres (hydrogen atoms) form the ice lattice. When the displacements of the hydrogen atoms from the O-O bond midpoints are depicted as arrows, it maps onto the spin arrangement in the NNLIF model ground state. (taken from ref. 22)*

Due to the ground state degeneracy, the systems displaying 'spin ice behaviour' typically do not show long range magnetic order down to temperatures where the thermal energy is lower than the energy barriers separating the degenerate states. Specific heat measurements[27,28] performed on $Dy_2Ti_2O_7$ confirmed that it in fact has some residual entropy at T = 0.4 K, providing evidence that $Dy_2Ti_2O_7$ is indeed an example of spin ice. Also, $Ho_2Ti_2O_7$ was proposed to be a spin ice material, based on neutron scattering and magnetization experiments[20]. Although there are some claims the system actually partially orders[29,30], the spin ice behaviour of $Ho_2Ti_2O_7$ is confirmed by recent specific heat[31], magnetization[32] and neutron scattering experiments, as well as by Monte Carlo simulations. Theoretically, the spins on the rare earth ions Ho^{3+} and Dy^{3+} were initially described as having weak ferromagnetic exchange interactions, leading to the spin ice behaviour. This model turned out to be too simple and was not able to reproduce the properties of the real spin ice systems[23,29]. Since Ho^{3+} and Dy^{3+} both have large magnetic moments of $\mu \approx 10\ \mu_B$, there are strong dipolar interactions between nearest neighbour moments. The dipolar interaction at nearest neighbour distances (D_{nn}) turns out to be about 2 K, the same order of magnitude as the energy scale of magnetic interactions in these materials, which is estimated from their Curie-Weiss temperatures, $|\Theta_{C.W.}| \sim 1$ K. As it turns out, the nearest neighbour exchange interaction in $Ho_2Ti_2O_7$ and $Dy_2Ti_2O_7$ is in fact *antiferro*magnetic. Since the dipolar interactions between the spins is ferromagnetic and somewhat stronger, however, the

'effective nearest neighbour interaction' is ferromagnetic, explaining the spin ice behaviour. Using models with dominant, long-range dipolar interactions, it is possible to achieve agreement with experimental results. The most important question that remains to be answered is which ground state do the real spin ice compounds actually freeze into.

A.2.1.IV) Spin glass

While liquid- or ice-like behaviour is observed in the rare earth titanate family, $Y_2Mo_2O_7$ shows yet another type of exotic low temperature behaviour, known as spin glass behaviour. This was quite a surprising find, since it was originally thought that spin glass behaviour would require in addition to magnetic frustration also some kind of chemical disorder[33,34]. Many spin glasses for example have two paramagnetic species in the system[35], satisfying this 'rule of thumb'. $Y_2Mo_2O_7$ has, however only one paramagnetic species in its structure, Mo^{4+} has electronic configuration $4d^2$ and thus S=1, while Y^{3+} has an empty d shell ($4d^0$) and is thus diamagnetic, like O^{2-}. Since it was also shown that $Y_2Mo_2O_7$ is a crystallographically well ordered compound[36], the question rose whether frustration alone might induce glassy behaviour. Also, the fact that the isotropic Heisenberg antiferromagnet model is believed to accurately describe $Y_2Mo_2O_7$ results in liquid-like behaviour being expected at lower temperatures, adding to the mystery of its actual glassy low-temperature state. $Y_2Mo_2O_7$ was found to freeze into a glassy state through a well characterized thermodynamic transition at a temperature of T_F =22.5 K, as established by bulk magnetization[37] and muon spin relaxation measurements[38]. General features of spin glass behaviour below T_F are history dependent bulk-magnetization, very slow dynamic response to a small magnetic field, yet still some spin dynamics down to very low temperatures and dynamics on a very broad range of length- and timescales, all of which are displayed by $Y_2Mo_2O_7$. It has been found[38,39] that the magnetic moments in $Y_2Mo_2O_7$ slow down very rapidly when approaching T_F from above, but do not develop long range order down to $0.1T_F$. The explanation for this glassy state came when XAFS[40] and NMR[41] experiments confirmed there is indeed a Mo-Mo bond length disorder in the $Y_2Mo_2O_7$ lattice and it was shown theoretically that the isotropic Heisenberg antiferromagnetic pyrochlore with weak bond disorder can freeze into a glassy state without developing long range order[42].

A.2.1.V) The 'spin-Teller' effect

The last magnetic pyrochlore system that will be adressed is $ZnCr_2O_4$. As mentioned above, the only paramagnetic species in this compound is Cr^{3+}, which has an electronic configuration $3d^3$ and S = $^3/_2$. The paramagnetic chromium-ions reside on a pyrochlore lattice, and are believed to be an excellent realization of the isotropic Heisenberg antiferromagnet. This means, as mentioned above, that the system is expected not to show long range magnetic order on the basis of this model. The Curie-Weiss temperature of $ZnCr_2O_4$ is $\Theta_{C.W.}$ = - 392 K, indicating strong antiferromagnetic interactions[43]. Assuming only nearest neighbour interactions are significant, this leads to an estimation of the nearest neighbour coupling of $J = [3\ \Theta_{C.W.}/zS(S+1)] = -52.3\ K$[44] ($z$ is the number of nearest neighbours) . And indeed as expected below $\Theta_{C.W.}$, with decreasing temperature the paramagnetic spins become increasingly correlated, but the system does remain in a spin liquid state, untill it undergoes a phase transition (see below)[45]. Now, since the five *3d* orbitals of Cr^{3+} are split up into a t_{2g} triplet and an e_g doublet (t_{2g} triplet is lowest in energy), the three electrons of Cr^{3+} occupy the three different t_{2g} orbitals with aligned spins, as predicted by Hund's rules. Considering the shape of the t_{2g} orbitals, which point towards the Cr^{3+} nearest neighbours, it can be concluded that the primary path for magnetic interactions between the Cr^{3+}-ions is direct exchange. As a result, further than nearest neighbour interactions are negligible in this system and more

importantly, the dominant nearest neighbour interactions are highly dependent on Cr^{3+}-ion motion, meaning there is a strong coupling lattice and spin degrees of freedom. Due to this coupling, $ZnCr_2O_4$ is able to relieve its frustration through a first order transition at $T_c \approx 12.5$ K, from a cubic into a tetragonal phase, which is consistent with theory[46,47]. This transition has been referred to as a spin-induced Jahn-Teller ('spin-Teller') effect[46,47] or a spin-Peierls like transtion, since the system 'sacrifices' some lattice energy to lower the magnetic energy (by introducing a gap in the magnetic excitation spectrum) and arrive in a state of lower total energy. One interesting feature of this system is the fact that just above T_c, the spins are correlated in hexagons, where each spin in the hexagon is either parallel or antiparallel to a common 'hexagon director'[48](fig. 6.). Each spin in the system is correlated in one hexagon only, meaning the system can be described as a system of weakly interaction hexagon-directors. There is some residual interaction due to the fact that the spins still fluctuate at these temperatures, which causes the hexagon-directors to have a very small fluctuating magnetic moment. More recently it was even shown that the spin correlation length above T_c can be probed by measuring phonon frequencies.

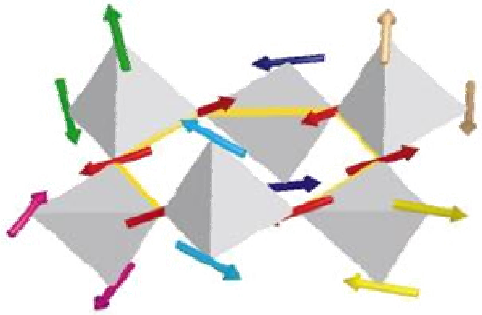

Fig. 6.: *Just above T_c in $ZnCr_2O_4$ the spins in a hexagon (red spins) are aligned along a common 'hexagon-director', with three spins pointing in each of both directions of the director. (taken from ref. 48)*

A.2.2.) Frustration in the triangular lattice

The only triangular lattice compound in this work is $CuFeO_2$. In this material, the Cu-ions are in the 1+ valence state, making them diamagnetic (electronic configuration $3d^{10}$). Since also O^{2-} is diamagnetic, Fe^{3+} is the only paramagnetic species in the lattice. The electronic configuration of the Fe^{3+}-ions is $3d^5$, resulting in $S = {}^5/_2$ and $L = 0$. The structure of $CuFeO_2$ consists of alternating stacked, hexagonal layers of Cu^+ and Fe^{3+}, with oxygen layers in between[49,50] (fig. 7.).

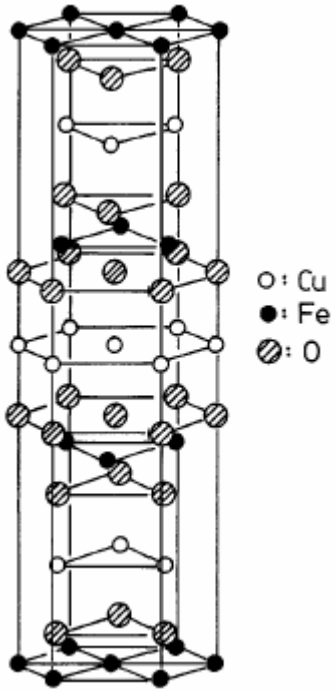

Fig. 7.: *The 'delafossite' structure of $CuFeO_2$. It consists of alternating layers of Cu^+ and Fe^{3+}, with intervening oxygen layers. The paramagnetic Fe^{3+}-ions span 2D triangular lattices in each layer. The Fe^{3+}-ions in one layer are above the center of the triangles formed by the Fe^{3+}-ions in the adjacent layers. (taken from ref.49)*

The Fe^{3+}-ions in one layer span a 2D triangular lattice (fig. 2.b.) and they are above the center of the triangles formed by the Fe^{3+}-ions in the neighbouring Fe-layer. Consequently, both the magnetic exchange interactions within a layer and between the layers are expected to be highly frustrated. For this highly frustrated geometry, a highly degenerate ground state is expected[51], as stated before however, any additional interactions can (in part) lift the degeneracy and select a complex magnetic ordering transition at low temperature. $CuFeO_2$ in fact shows two successive magnetic transitions, at $T_{N1} \approx 16$ K the system goes into a partially disordered (PD) phase and at $T_{N2} \approx 11$ K there is a transition into a long range ordered '4-sublattice' magnetic phase. Again, as usual for frustrated magnets, the transition temperatures lie far below the energy scale set by the Curie-Weiss temperature, $\Theta_{C.W.} \approx -90$ K for $CuFeO_2$[50,52]. In the PD state the spins form a sinusoidially-amplitude-modulated magnetic structure, meaning the sign and magnitude of the ordered parts of the spins, which are parallel

to the c-axis, are described by a sinusoidal wave in the (qq0) direction[53,54] (fig. 8.b.). The '4-sublattice' (↑↑↓↓) structure is depicted in fig. 8.a., here the spins arrange in 4 sublattices, with alternating two spins parallel and two anti-parallel to the c-axis. The (↑↑↓↓) structure can be seen in the ($^1/_4{}^1/_4{}^3/_2$) direction. What is quite unusual here, is that although the spins of Fe^{3+} (which is in an orbital singlet state, $L = 0$) are expected to be isotropic (Heisenberg), they show Ising behaviour in aligning collinear with the c-axis (though Fe^{3+} is 'notorious' for this). This, especially because one intuitively expects the system would be able to relieve some frustration if the spins were isotropic. Intuitively, one expects a configuration with canted spins (imagine a 120°-like correlation, possible with isotropic spins) would reduce the frustration and the magnetic exchange energy substantially (as long as the anisotropy is not too strong), however, in exhibiting Ising-like behaviour the system seems to be in the state of maximum frustration. This is the reverse situation as compared to the pyrochlore antiferromagnet case, where having local Ising spins would reduce the frustration substantially and isotropic Heisenberg spins induce maximum frustration. Theory has been able to account for the low-temperature phases of $CuFeO_2$ by using models which take next-nearest-neighbour interactions within layers and nearest-neighbours interactions between layers into account[55]. However, origin of the Ising-like behaviour is still under debate.

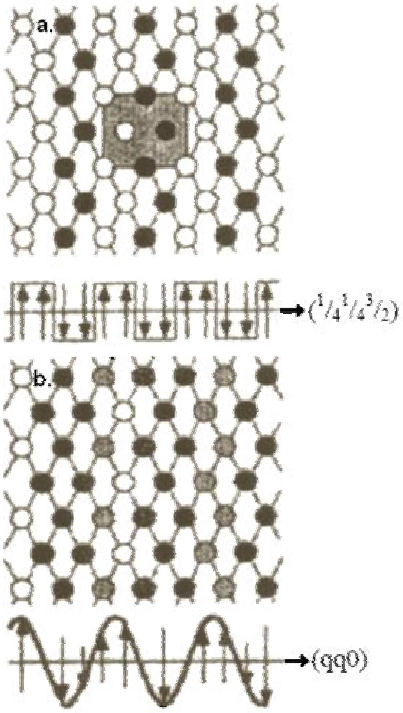

Fig. 8.: a) *The magnetic structure of the Fe^{3+} moments in one layer in the lowest temperature '4-sublattice' phase.* ***b)*** *The magnetic structure in the intermediate phase, where the ordered part of the spins varies sinusoidally in both sign (direction) and amplitude in the qq0-direction. In both drawings are in the top-view, looking along the c-axis. (taken from ref. 53)*

Of all the compounds that were adressed in this introduction, the most important features are listed in table 1 below, for quick reference.

Table 1

Compound	Lattice	Dimensio-nality	Magn. species, elec. config.	Spin anisotropy	Low temp. behaviour
$Tb_2Ti_2O_7$	$A_2B_2O_7$, A-site : pyrochlore	3D	Tb^{3+}, $4f^8$	Local [111] Ising spins	Spin liquid
$Gd_2Ti_2O_7$	$A_2B_2O_7$, A-site : pyrochlore	3D	Gd^{3+}, $4f^7$	Isotropic (Heisenberg)	Partial ordering
$Ho_2Ti_2O_7$	$A_2B_2O_7$, A-site : pyrochlore	3D	Ho^{3+}, $4f^{10}$	Local [111] Ising spins	Spin ice
$Dy_2Ti_2O_7$	$A_2B_2O_7$, A-site : pyrochlore	3D	Dy^{3+}, $4f^9$	Local [111] Ising spins	Spin ice
$Y_2Mo_2O_7$	$A_2B_2O_7$, B-site : pyrochlore	3D	Mo^{4+}, $4d^2$	Isotropic (Heisenberg)	Spin glass
$ZnCr_2O_4$	AB_2O_4, B-site: pyrochlore	3D	Cr^{3+}, $3d^3$	Aligned // to director	'spin-Teller' transition
$CuFeO_2$	Layered triangular	Quasi-2D	Fe^{3+}, $3d^5$	Ising spins // to c-axis	Incommensu-rate phases

A.3.) Motivation for this work

The most interesting thing about these frustrated systems is their unpredictability and extremely diverse nature. The possibility of finding new, exotic magnetic ground states and exploring their properties is a strong motivation for many condensed matter scientists to work on this phenomenon, making this field a popular theme in condensed matter science today. Although the ground states of frustrated systems have received and are receiving a lot of scientific attention, surprisingly little effort has been made to clarify the excitations in such systems. One would expect that if a system has a large number of (nearly) degenerate ground states, there will also be low-lying excitations connecting these states. For the highly frustrated magnets investigated in this work, a high density of dispersionless, low energy excitations ('soft modes' or 'zero modes') is thus expected. In an attempt to gain more insight in the exotic magnetic behaviour of these systems, they will be investigated using inelastic light scattering (Raman spectroscopy). To see if these low energy excitations can be excited using photons and if so, what information about the system this can yield. This work is done as a master-thesis project, with the main idea being to experience the field of materials research. The project is set up to go through a full research-cycle during the final master year, starting from a literature study, through material synthesis (performed in an external laboratory), material characterization and preparation, experimental setup, sample measurements, data analysis and finally to interpretation and understanding of results. The project is not designed to be limited to a single year of research and most likely there will many new questions at the end of the first year, making an extension to the project a possibility.

B.) Single crystal growth using the floating zone technique

As a first step in this research, an attempt has been made to grow high quality single crystals of all the compounds described in the introduction above. This has been done by the so-called 'floating' or molten zone technique, using an optical image furnace. This part of the research (comprising approximately 3 months) was conducted in Paris, at the 'Laboratoire de Physico-Chimie de l'Etat Solide' (LPCES) of the Université Paris-Sud XI, in the solid state research group headed by professor Alexandre Revcolevschi. The goal of the stay in Paris was, next to growing the compounds mentioned above using this technique, to learn about the methods involved in growing high-quality single crystals, in particular about the floating zone technique and to experience the materials synthesis process. The experiments in France were conducted in cooperation with Guy Dhalenne, a full-time researcher of the LPCES with great experience in crystal growth in general and with oxides in particular. At the LPCES, there were two optical image furnaces that were used in the crystal growth experiments, the NEC SC-N15HD and the FZ-T-4000-H-II-P P Optical Floating Zone Furnace of Crystal Systems Inc. The general characteristics of the technique are explained here, while the details of each growth are given in the sample specific paragraphs.

In the NEC SC-N15HD optical image furnace (fig. 9), two semi-ellipsoidal mirrors are used to bring the light of two 1500 Watt (100 V) halogen lamps to a common focus ('hot zone'), which is about 1 cm in diameter. The sample consists of two parts, a seed rod, which is preferably a small single crystal of the compound of interest, and a feed rod, which is a polycrystalline bar, consisting of the isostatically pressed and subsequently sintered powder of the same compound. The feed rod is suspended from the upper drive shaft, the seed rod is placed on the lower drive shaft, and the rods are brought close together at the common focus of the mirrors. This common focus is inside an isolated quartz tube, which allows for the growth to be conducted in a wide variety of atmospheres and pressures.

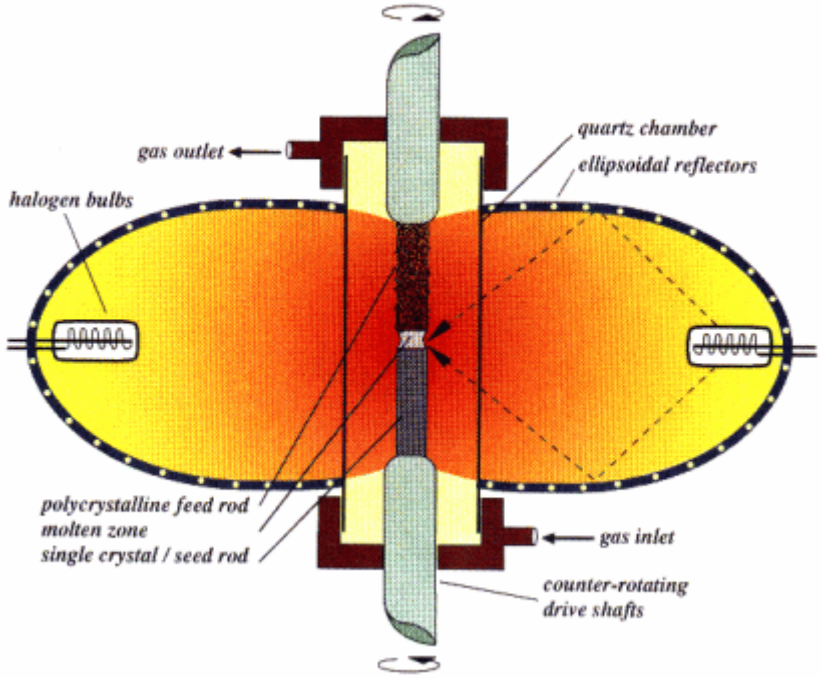

***Fig. 9**: Schematic drawing of single crystal growth using an optical image furnace. Light from the two halogen bulbs is focused in the hot zone by two ellipsoidal mirrors, creating a molten zone between the counter-rotating feed and seed rods. By synchronously lowering these rods through the hot zone, a single crystal is grown from the seed rod. Since growth is conducted in an isolated quartz tube, it can be conducted in many different atmospheres and at a wide variety of pressures. (taken from http://www.physics.uc.edu/~jph/emma/growth.html)*

The feed and seed rods are both counter-rotated at a rate of about 20 to 30 rpm to ensure homogeneous heating of the rods as well as efficient mixing and thus homogeneity in the molten zone. The rate of counter-rotation is an optimum value. At too low rotation rates the efficient mixing and homogeneous heating of the floating zone are suppressed, while too high rotation rates may cause crystal defects due to an instable floating zone. The specific optimum is slightly viscosity- and thus compound-dependent, but the empirical rule is that most compounds have an optimum between ~ 20 and 30 rpm. The temperature of the sample at the focus can be controlled by varying the voltage applied over the halogen lamps, because this varies the brightness of the lamps and thus the intensity of the light at the focus. Thus, the voltage is set to the value corresponding to the melting temperature of the compound. Since the top of the seed rod (ideally a small piece of single crystal of the compound, having a desirable growth axis) and the bottom of the feed rod are in the hot zone, they melt. Next, the molten ends of the rods are carefully brought into contact, creating a liquid zone ('floating zone') of the compound, connecting the two rods. To actually grow the single crystal from the seed, the seed and feed rods are lowered synchronously through the hot zone, at a very slow rate of typically a few mm h^{-1}. As the sample is lowered, the lowest part of the floating zone is moved out of the hot zone, causing it to solidify on top of the seed rod. Since the microscopic preference of the cooling melt is to solidify with the same symmetry as the seed rod, the crystal grows in single crystalline form. Simultaneously, the lowest still solid part of the feed rod is moved into the hot zone, causing it to melt and complement the floating zone. As the hot zone is moved along the sample, the seed rod slowly grows into a large single crystal, while the feed rod is slowly 'consumed' by the floating zone. The exact growth rate is again an optimum value. The empirical rule of thumb here is that the slower the growth rate, the better the grown crystal. On the other hand, there is of course the issue of time-efficiency, growing a 60 mm crystal at a rate of 0.5 mm h^{-1} will take 120 hours. Consequently, the typical growth rates are in the order of a few mm h^{-1}.

The design of the CSI FZ-T-4000-H-II-P P Optical Floating Zone Furnace is very similar to that of the NEC SC-N15HD furnace and the working principle is exactly the same. There are only two mayor differences between the two. Firstly, the CSI furnace has 4 halogen lamps and ellipsoidal mirrors, in contrast to the NEC's 2. Secondly, instead of moving the feed and the seed rod downwards through the hot zone, the CSI furnace moves the lamps and mirrors and thus the hot zone upwards. The effect is the same as in the NEC furnace, the feed rod is slowly 'consumed', as it melts when the hot zone passes, while a crystal grows from the seed rod, as the cooling melt solidifies when the hot zone moves upwards.

B.1.) Growth of terbium titanate ($Tb_2Ti_2O_7$) single crystals

Initially, the terbium titanate was synthesized in polycrystalline form through a solid state reaction between the starting oxides:

$$Tb_4O_7 + 4\ TiO_2 \rightarrow 2\ Tb_2Ti_2O_{7,5} \rightarrow 2\ Tb_2Ti_2O_7 + \tfrac{1}{2}\ O_2 \uparrow$$

Two rounds of synthesis were performed, $Tb_2Ti_2O_7$ crystals A, B and C were grown using the samples from the first round, which is described here. $Tb_2Ti_2O_7$ crystal D was grown using a sample from the second synthesis round, which is described before section B.1.4.

First synthesis round: The first step of the synthesis was the thorough grinding and mixing of stoichiometric amounts of Tb_4O_7 (Alfa Aesar, 99.99% pure, 14.0121 g) and TiO_2 (Cerac Inc., 99.9 % pure, 5.9884 g) and the subsequent heating of the mixture for 20 hours at 990 °C, in air. Next, the resulting powder was ground and isostatically pressed into two rods, 10 and 7

mm in diameter and 70 and 60 mm in length, respectively. The rods were then heated in air at 1200°C for 48 hours to complete the reaction, after which they were again ground and isostatically pressed into two new rods, 6 mm in diameter and approximately 50 and 60 mm in length. These rods were subsequently sintered at 1320 °C for 48 hours to increase the sample density. The ideal situation of course is for the feed rod to have the same density as the crystal to be grown. In most cases in this work, the density of the feed rod is quite comparable to the density of the crystal to be grown, illustrated by the fact that the crystal diameter is comparable to the diameter of the feed rod and by the fact that the moving speed of the upper en lower rods are the same. After this, the polycrystalline rods were used to grow single crystals using one of the optical image furnaces of the LPCES, the NEC SC-N15HD or the CSI FZ-T-4000-H-II-P P.

B.1.1.) Crystal $Tb_2Ti_2O_7$-A

For the growth of the $Tb_2Ti_2O_7$-A crystal, a $Tb_2Ti_2O_7$ seed single crystal of unknown orientation, which was previously grown at the 'Laboratoire de Physico-Chimie de l'Etat Solide' (LPCES), was used. As the feed rod, the $Tb_2Ti_2O_7$ bar of 60 mm in length and 6 mm in diameter, grown in the first synthesis round was used. The feed and the seed rod were placed in the NEC SC-N15HD image furnace and were both counter-rotated at a rate of 26-27 rpm and a floating zone of liquid $Tb_2Ti_2O_7$ was established between the two rods by applying a voltage of 83.2 V (melting point of $Tb_2Ti_2O_7$ is ≈ 1850°C) to the halogen lamps. Both rods were then synchronously lowered through the hot zone at a rate of approximately 3 mm h^{-1} and the growth was conducted under an O_2 atmosphere. The process was stopped when one of the halogen bulbs burned, at which point about half of the feed rod had been 'consumed'. Nevertheless, a large single crystal had been grown, about 40 mm in length and about 3 mm in diameter (fig 10.a.). The crystal was transparent to light with a brown-red colour and it had developed several facets during the growth.

Fig. 10: a. *$Tb_2Ti_2O_7$-A crystal* ***b.*** *$Tb_2Ti_2O_7$-B crystal*

c.*$Tb_2Ti_2O_7$-B crystal*

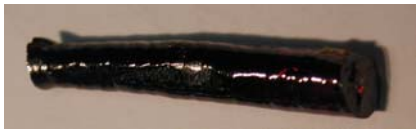

B.1.2.) Crystal $Tb_2Ti_2O_7$-B

After replacing the halogen lamps, the remaining part of the feed rod of the first $Tb_2Ti_2O_7$ growth was used to grow a second $Tb_2Ti_2O_7$ crystal, using the same seed rod as in the first growth (after the first crystal was grown, the original seed was sawed off). Prior to the growth of this second crystal the position of the halogen lamps was fine-tuned to achieve the same temperature in the hot zone at the same applied voltage. The feed and the seed rod were placed in the NEC SC-N15HD image furnace and were both counter-rotated at a rate of 26-27 rpm. Applying a voltage of 83.1 V (melting point of $Tb_2Ti_2O_7$ is ≈ 1850°C) to the halogen lamps, a floating zone was established and the second crystal was grown by synchronously lowering both the feed and the seed rod through the hot zone at a rate of about 3 mm h^{-1}, again under an O_2 atmosphere. In this way a single crystal of about 50 mm in length was grown, which shows 2 facets but which is not transparent, but has a dark, opaque appearance. Due to

density fluctuations along the axis of the feed rod, the diameter of the grown crystal varies along the crystal axis, with an average diameter of approximately 4 mm (fig. 10.b.). This illustrates the influence of the feed rod density on the crystal to be grown and highlights the importance of the sintering step in the sample preparation.

B.1.3.) Crystal $Tb_2Ti_2O_7$-C

The third $Tb_2Ti_2O_7$ crystal was grown using the second bar of the first synthesis round, which was 50 mm in length and 6 mm in diameter, as the feed rod. The same seed as used before was used and under similar conditions (NEC SC-N15HD image furnace, voltage 81.2 V (melting point of $Tb_2Ti_2O_7$ is ≈ 1850°C), counter rotation 26-27 rpm, feed and seed speed 3 mm h^{-1}, O_2 atmosphere) a single crystal about 35 mm in length and was grown. Again, due to density fluctuations along the axis of the feed rod, the diameter of the grown crystal varies along the crystal axis, with an average diameter of 4 mm.

Second synthesis round: Following the same procedure as in the first synthesis round, a second $Tb_2Ti_2O_7$ sample was synthesized, again by mixing and grinding 14.0121 g of Tb_4O_7 (Alfa Aesar, 99.99% pure) and 5.9878 g of TiO_2 (Cerac Inc., 99.9 % pure), after which the mixture was fired in air, at 990°C, for 40 hours. The resulting powder was ground and isostatically pressed into two rods, both 65 mm in length and 10 and 7 mm in diameter, respectively. These rods were then heated in air, at 1300°C, for 24 hours, and subsequently ground into powder again. This powder was pressed into two new rods, both 6 mm in diameter and approximately 50 and 60 mm in length, respectively. Finally, these rods were sintered in air, at 1265 °C, for 48 hours.

B.1.4.) Crystal $Tb_2Ti_2O_7$-D

The fourth $Tb_2Ti_2O_7$ crystal was grown using the 50 mm long sintered bar of the second synthesis, which was 6 mm in diameter, as the feed rod. As a seed, a 6 mm long, transparent piece of the $Tb_2Ti_2O_7$-C crystal that was grown, was used. The diameter of this part of the crystal was fairly constant at about 4 mm. Both the feed and the seed rod were then mounted in the CSI FZ-T-4000-H-II-P P image furnace. Next, the feed and seed rod were both counter rotated at a rate of 24-18 rpm and a floating zone was established by applying a voltage of 79.1 V (melting point of $Tb_2Ti_2O_7$ is ≈ 1850°C) to the 4 halogen lamps of the furnace. The mirrors and lamps were moved upwards at a rate of 1.8 mm h^{-1} to achieve crystal growth, while under an O_2 atmosphere. In this way a large single crystal, 4 mm in diameter and 35 mm in length, was grown, showing multiple facets and being transparent to light with a brown-reddish colour (fig.10.c).

B.2.) Growth of gadolinium titanate ($Gd_2Ti_2O_7$) single crystals

Initially, gadolinium titanate was synthesized in polycrystalline form using a solid state reaction between the starting oxides:

$$Gd_2O_3 + 2\ TiO_2 \rightarrow Gd_2Ti_2O_7$$

The first step in the synthesis was the thorough grinding and mixing of stoichiometric amounts of Gd_2O_3 (Alfa Aesar, 99.99% pure, 13.8800 g) and TiO_2 (Cerac, Inc. 99.9 % pure, 6.1201 g) and subsequently firing the mixture for 48 hours at 990°C, in air. Next, the resulting powder was ground and isostatically pressed into two rods, 10 and 7 mm in diameter and 70

and 40 mm in length, respectively. The rods were then heated in air at 1200°C for 24 hours to complete the reaction, after which they were again thoroughly ground into a powder. This powder was subsequently pressed into two new rods, both approximately 70 mm in length and 6 mm in diameter. These rods were then sintered at 1265°C for 48 hours in air.

B.2.1.) Crystal $Gd_2Ti_2O_7$-A

The growth of the first $Gd_2Ti_2O_7$ crystal was performed using a small $Gd_2Ti_2O_7$ single crystal of unknown orientation as a seed. This seed crystal was previously grown at the LPCES. As the feed rod, one of the $Gd_2Ti_2O_7$ bars of 70 mm in length and 6 mm in diameter was used. The feed and the seed rod were placed in the NEC SC-N15HD image furnace and were both counter-rotated at a rate of 26-27 rpm, after which a floating zone of liquid $Gd_2Ti_2O_7$ was established between the two rods by applying a voltage of 78.8 V (melting point of $Gd_2Ti_2O_7$ is ≈ 1820°C) to the halogen lamps. Both rods were then synchronously lowered through the hot zone at a rate of approximately 3 mm h^{-1}. The growth process, which was conducted under an O_2 atmosphere, was stopped when the feed and the seed rod were no longer connected through a floating zone. This occurred naturally and was caused by the fact that the feeding rod had many large cracks when melting, which, when close enough to the hot zone, got filled by liquid from the floating zone. The liquid was thus removed from the hot zone, breaking the liquid bridge between the rods. Nevertheless, a $Gd_2Ti_2O_7$ single crystal of about 35 mm length and about 4 mm diameter had been grown. The crystal was transparent to light with a brown-yellowish colour and it had developed several facets during the growth.

B.2.2.) Crystal $Gd_2Ti_2O_7$-B

During the first crystal growth, it became evident that the feed rod exhibits multiple large cracks when melting. This results in a large variation of the newly grown crystal's diameter when no manual adjustments to the feed rod's position are made and can in the worst case result in the floating zone being interrupted. Since a large part of the crystal growth takes place when it is unattended (the growth of a 60 mm crystal at 3 mm h^{-1} takes 20 hours), the development of such cracks must be avoided. Since the occurrence of these cracks is most probably due to the sintering temperature being to low (1265ºC), the second $Gd_2Ti_2O_7$ bar was again ground into a powder, pressed into a new rod of diameter 6 mm and length 63 mm, and re-sintered in air, at a temperature of 1350ºC, for 30 hours. Then it was placed in the CSI FZ-T-4000-H-II-P P image furnace. The re-sintered $Gd_2Ti_2O_7$ bar was used as a feed rod for the second $Gd_2Ti_2O_7$ crystal growth, using the same seed as in the first $Gd_2Ti_2O_7$ growth experiment. The seed rod was rotated at 27 rpm and a floating zone of liquid $Gd_2Ti_2O_7$ was established between the feed and seed rod by applying a voltage of 76.8 V (melting point of $Gd_2Ti_2O_7$ is ≈ 1820°C) to the halogen lamps, under an O_2 atmosphere. The mirrors and lamps were moved upwards at a rate of 6 mm h^{-1} to achieve crystal growth. In order to maintain a constant crystal diameter during growth, the feed rod was lowered at a rate of 1.5 mm h^{-1}. After 24 mm of crystal growth, the growth rate (upwards movement of the lamps and mirrors) was lowered to 1.7 mm h^{-1}, while the lowering speed of the feeding rod was decreased to 0.35 mm h^{-1}. In this way, a large single crystal of $Gd_2Ti_2O_7$ was grown with a diameter of 4 mm and a length of 60 mm (fig. 11). The crystal shows several facets that had developed during the growth and it was transparent to light with a dark brownish colour.

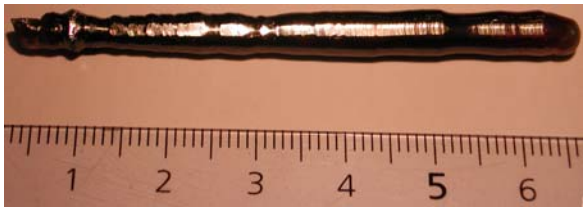

Fig. 11: *The crystal $Gd_2Ti_2O_7$-B. The light reflection emphasizes the natural facet on the crystal.*

B.3.) Growth of holmium titanate ($Ho_2Ti_2O_7$) single crystals

As for all the titanates, the holmium titanate was initially synthesized in polycrystalline form by having the starting oxides undergo a solid state reaction:

$$Ho_2O_3 + 2\ TiO_2 \rightarrow Ho_2Ti_2O_7$$

As before, the first step of the synthesis was the thorough grinding and mixing of stoichiometric amounts of Ho_2O_3 (Alfa Aesar, 99.9% pure, 21.0852 g) and TiO_2 (Cerac, Inc. 99.9 % pure, 8.9148 g) and subsequently heating the mixture in air, for 48 hours, at 990°C. Next, the resulting pinkish powder was ground and isostatically pressed into two rods, both 80 mm in length and 10 and 7 mm in diameter, respectively. The rods were then heated in air at 1200°C for 48 hours to complete the reaction, after which they were again thoroughly ground into a slightly yellowish powder. This powder was then isostatically pressed into two 6 mm diameter rods of 75 and 90 mm length, respectively. These rods were subsequently sintered at 1350°C for 30 hours, in an air atmosphere.

B.3.1.) Crystal $Ho_2Ti_2O_7$-A

Since there was no previously grown seed available for $Ho_2Ti_2O_7$, a small piece of approximately 6 mm length was cut from the 75 mm long sintered, polycrystalline $Ho_2Ti_2O_7$ bar, to be used as the seed rod. The remainder of the 75 mm $Ho_2Ti_2O_7$ bar, which was 6 mm in diameter, was used as the feed rod. The feed and the seed rod were placed in the CSI FZ-T-4000-H-II-P P image furnace and were both counter-rotated a rate of 20-25 rpm. After putting the sample under an O_2 atmosphere, a floating zone was established between the rods by applying a voltage of 82.5 V (melting point of $Ho_2Ti_2O_7$ is ≈ 1830°C) to the halogen lamps. The mirrors and lamps were then synchronously moved upwards at a rate of 2 mm h^{-1}. In this way a large $Ho_2Ti_2O_7$ single crystal of 45 mm length and 5 mm diameter was grown, which is transparent with a yellow colour and shows two facets.

B.3.2.) Crystal $Ho_2Ti_2O_7$-B

For the second growth of a $Ho_2Ti_2O_7$, a small piece of approximately 6 mm length was cut from one of the 90 mm long sintered, polycrystalline $Ho_2Ti_2O_7$ bar, to be used as the seed rod. The remainder of the 90 mm long $Ho_2Ti_2O_7$ bar, which was 6 mm in diameter, was used as the feed rod. The feed and the seed rod were placed in the CSI FZ-T-4000-H-II-P P Optical Floating Zone Furnace and were both counter-rotated a rate of 22-25 rpm. The sample was put under an O_2 atmosphere and a floating zone was established between the rods by applying a voltage of 82.6 V (melting point of $Ho_2Ti_2O_7$ is ≈ 1830°C) to the halogen lamps. The mirrors and lamps were then synchronously moved upwards at a rate of 1.8 mm h^{-1}. In this way a large $Ho_2Ti_2O_7$ single crystal of 65 mm length and 5 mm diameter was grown, which is transparent with a yellow colour and shows two facets (fig. 12).

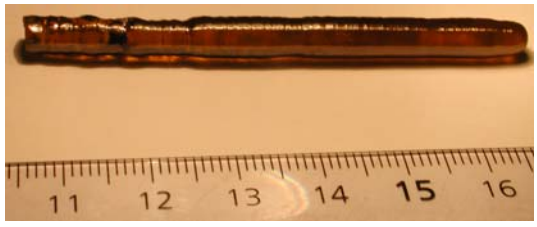

Fig. 12: *Crystal $Ho_2Ti_2O_7$-B. Its yellow colour, transparency and dimensions are clearly visible.*

B.4.) Growth of dysprosium titanate ($Dy_2Ti_2O_7$) single crystals

Again, the dysprosium titanate was first synthesized in polycrystalline form using a solid state reaction between the starting oxides:

$$Dy_2O_3 + 2\ TiO_2 \rightarrow Dy_2Ti_2O_7$$

The first step of the synthesis was the thorough grinding and mixing of stoichiometric amounts of Dy_2O_3 (Alfa Aesar, 99.9% pure, 21.0038 g) and TiO_2 (Cerac, Inc. 99.9 % pure, 8.9962 g) and the subsequent heating of the mixture for 48 hours at 990°C, in air. Next, the resulting powder was ground and isostatically pressed into three rods, all three of them were 7 mm in diameter and they were 80, 75 and 40 mm in length, respectively. The rods were then heated in air at 1200°C for 48 hours to complete the reaction, after which they were again thoroughly ground into a powder. The obtained white powder was subsequently pressed into two new rods, both 6 mm in diameter and approximately 90 mm in length, which were then sintered at 1350°C for 30 hours in air.

B.4.1.) Crystal $Dy_2Ti_2O_7$-A

Since there was also no previously grown seed available for $Dy_2Ti_2O_7$, a small piece of approximately 7 mm length was cut from one of the 90 mm long sintered, polycrystalline $Dy_2Ti_2O_7$ bars, to be used as the seed rod. The remainder of the 90 mm $Dy_2Ti_2O_7$ bar, which was 6 mm in diameter, was used as the feed rod. The feed and the seed rod were placed in the CSI FZ-T-4000-H-II-P P image furnace and were both counter-rotated a rate of 24-26 rpm. A floating zone was established between the rods by applying a voltage of 81.5 V (melting point of $Dy_2Ti_2O_7$ is ≈ 1850°C) to the halogen lamps. The mirrors and lamps were then synchronously moved upwards at a rate of 3.5 mm h^{-1}, while the sample was under an O_2 atmosphere. In this way a large single crystal of 40 mm length and 5 mm diameter was grown, showing two facets. The crystal was divided into two parts, about 30 and 10 mm. The $Dy_2Ti_2O_7$ crystal is transparent with a yellow colour and there is a crack along the growth axis for the larger part of the crystal.

B.4.2.) Crystal $Dy_2Ti_2O_7$-B

For the growth of the second $Dy_2Ti_2O_7$ crystal, the remaining piece of the $Dy_2Ti_2O_7$ bar that was used as the feed rod for the growth of the first crystal was used as a seed. The other 90 mm long, polycrystalline $Dy_2Ti_2O_7$ bar was used a as feed rod for this growth. The rods were then placed in the CSI FZ-T-4000-H-II-P P image furnace and were both counter-rotated at a rate of 20-21 rpm and put under an O_2 atmosphere. A floating zone was established between the rods by applying a voltage of 82.3 V (melting point of $Dy_2Ti_2O_7$ is ≈ 1850°C) to the halogen lamps. The mirrors and lamps were then synchronously moved upwards at a rate of 1.5 mm h^{-1}. In this way, a large single crystal of $Dy_2Ti_2O_7$ was grown, which showed four facets. The crystal is 60 mm in length and 5 mm in diameter and is transparent with a yellow-brown colour (fig. 13).

Fig. 13: *The $Dy_2Ti_2O_7$-B crystal is transparent with a yellow-brownish colour.*

Finally, to illustrate the importance of exact stoichiometry in the synthesis of single crystals, the phase diagram of the $Dy_2O_3 \cdot TiO_2$ system is depicted in fig. 14. As can been seen in the picture, in order to have a pure $Dy_2Ti_2O_7$ phase, one should create a system that is exactly on the pure $Dy_2Ti_2O_7$-line in the phase diagram (the vertical line at 66.667 mol % of TiO_2). This means the starting oxides Dy_2O_3 and TiO_2 should be mixed in a ratio 1:2, as was done in the synthesis described above. In that case (assuming negligible evaporation of the compounds) the system in the molten (liquid) phase is exactly above the pure $Dy_2Ti_2O_7$-line in the phase diagram and when growing a single crystal from the cooling melt the system the system solidifies in a pure $Dy_2Ti_2O_7$ crystal (traveling along the indicated arrow in the phase diagram). As can be seen from the picture, slight nonstoichiometry (deviation from the $Dy_2Ti_2O_7$-line) already causes the coexistence of two phases.

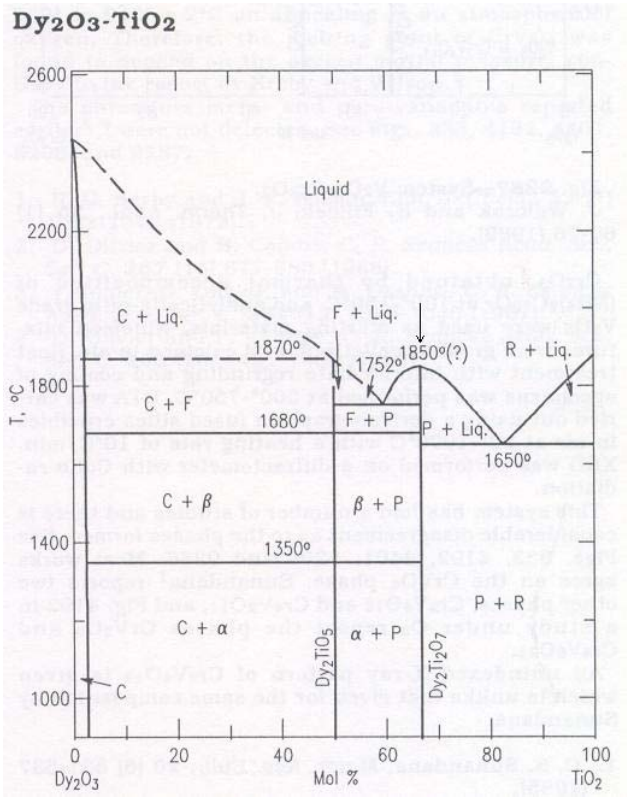

Fig. 14: *Phase diagram of the $Dy_2O_3 \cdot TiO_2$ system. It is clear from the picture that in only a very narrow range of stoichiometry a purely $Dy_2Ti_2O_7$ phase is formed. Symbols: P = $Dy_2Ti_2O_7$ (pyrochlore structure), C = solid solution based on Dy_2O_3, F = cubic solid solution with fluorite structure, R = rutile (TiO_2) structure. α and β are low and high temperature forms of Dy_2TiO_5. (taken from 'Phase diagrams for ceramists', Volume XI, Edited and Published by The American Ceramic Society (1995),* ***ISBN:*** *0944904041)*

B.5.) Growth of a cuprous ferrite ($CuFeO_2$) single crystal

The most obvious way of making $CuFeO_2$ is to synthesize it directly from the starting oxides Cu_2O and Fe_2O_3 through a solid-state reaction under an argon atmosphere. Zhao *et al.* reported[56], however, that using this method of preparation, traces of metallic copper impurities can be formed. This is assumed to be caused by the reduction of Cu_2O in the argon atmosphere, through the reaction:

$$2\ Cu_2O \rightarrow 4\ Cu + O_2 \uparrow$$

Zhao *et al.* also report an alternative synthesis of $CuFeO_2$, which avoids the problem of copper impurities. This alternative method has been used to synthesize the $CuFeO_2$ compound for our experiments.

For this alternative synthesis, CuO (Chempur, 99.99% pure, 9.9811 g) and Fe_2O_3 (Alfa Aesar, 99.99% pure, 10.0189 g) were used as the starting materials. They were carefully mixed in the molar ratio of 2:1 and the powder mixture was subsequently prefired in air at 835°C for 16 h. The following reaction takes place during prefiring:

$$2\ CuO + Fe_2O_3 \rightarrow CuFe_2O_4 + CuO$$

An analysis of the resulting powder using powder X-Ray Diffraction (XRD) confirmed that the product powder consisted of $CuFe_2O_4$ and CuO (All the powder XRD measurements in

this work were performed on the Philips X'Pert Diffractometer of the LPCES, in the spinner mode). Next, 10 grams of the prefired powder was thoroughly ground and mixed again, and heated at 950°C for 48 hours in an Ar + 15 % H_2 atmosphere. During this treatment the powder had reduced, since it was clear that metallic copper had been formed.

To prevent the reduction of the CuO, the remaining 10 grams of the prefired powder was heated at 950°C for 24 hours in a N_2 atmosphere, as was done by Zhao *et al*. XRD of the resulting powder confirmed its main phase to be $CuFeO_2$, with some traces of Cu_2O and Fe_2O_3 still present. To complete the reaction, the powder was isostatically pressed into a bar, 7 mm in diameter and 80 mm in length which was subsequently heated at 950°C in a N_2 atmosphere for another 24 hours. After this thermal treatment the bar was ground into a powder again, and the powder was analyzed by XRD, which confirmed the powder was single phase $CuFeO_2$. After isostatically pressing the powder into a new bar, 7 mm in diameter and 67 mm in length, it was sintered at 950°C in an O_2-filtered Ar atmosphere for 48 hours. Upon retrieval of the bar, it turned out the surface had reduced to metallic copper. This unwanted reduction of the product is ascribed to the O_2-purification of the Ar gas and the long heating time, since sintering in Ar gas posed no problem for Zhao *et al*.

A new synthesis round was started, by mixing stoichiometric amounts of CuO (Chempur, 99.99% pure, 9.9811 g) and Fe_2O_3 (Alfa Aesar, 99.99% pure, 10.0189 g) in the molar ratio 2:1. The carefully mixed powder was thoroughly grounded and subsequently prefired in air at 835°C for 17 h to obtain a mixture of the product, $CuFe_2O_4$, and traces of the unreacted starting compounds, which was confirmed by XRD (Fig. 15).

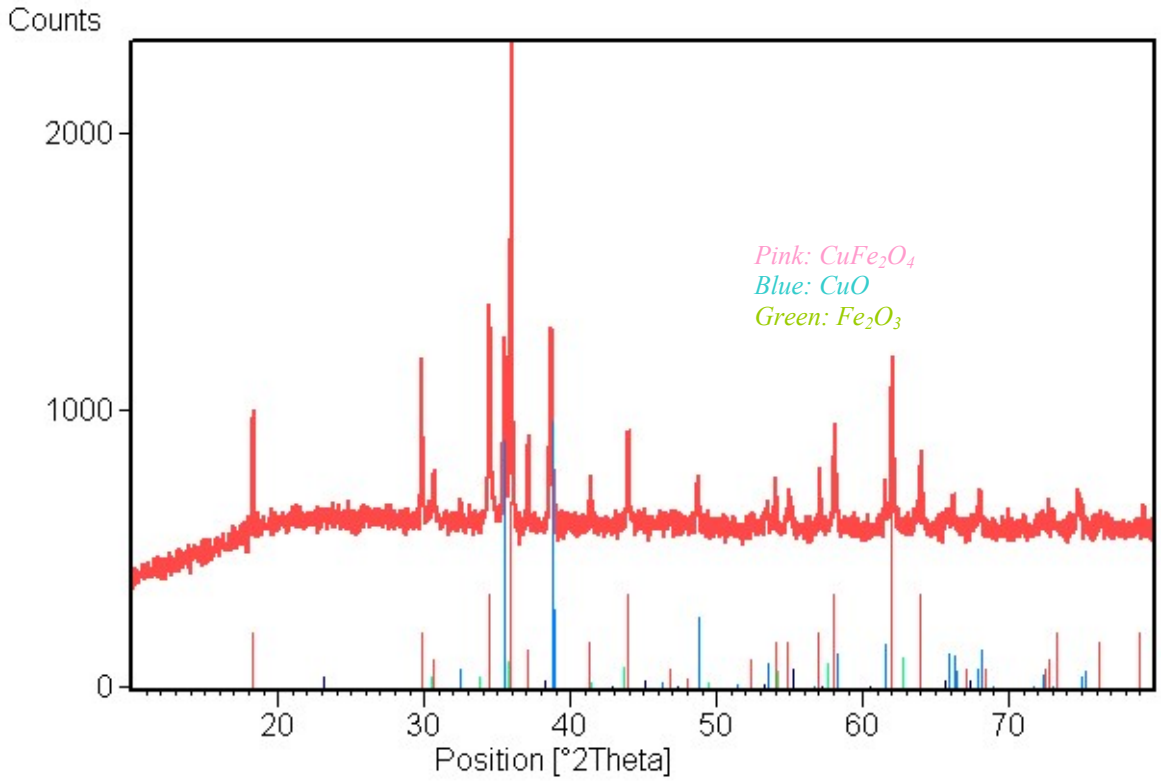

Fig. 15: *X-ray powder diffraction spectrum of the prefired mixture (in red). The coloured lines are the measured diffraction peaks from references, where the different colours represent the different compounds in the mixture, and the lengths indicate relative intensities.*

The next step in the synthesis process was the isostatic pressing of the prefired powder into three bars of approximately 45 mm length and 6 mm diameter. The bars were then heated at 950°C in a N_2 atmosphere for 24 hours and afterwards ground back into powder. The powder was analyzed by XRD, confirming it to be almost single phase $CuFeO_2$, with a very small trace of FeO (Fig. 16).

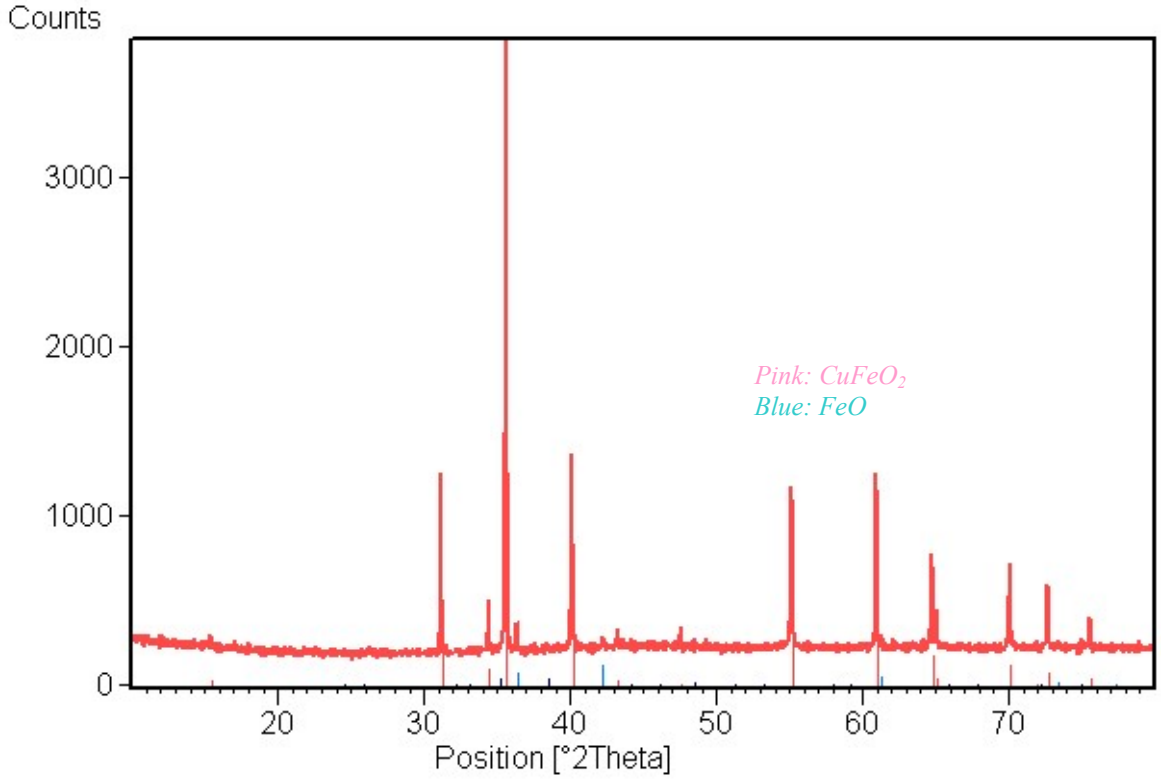

Fig. 16: *X -ray powder diffraction spectrum of the mixture, after the second heating treatment (in red). The coloured peaks are the measured diffraction peaks from references, where the pink peaks represent the diffraction peaks of $CuFeO_2$, and the blue peaks represent FeO reflections.*

To complete the reaction, the powder was again isostatically pressed into two bars of 6 mm diameter and 65 and 55 mm in length, respectively. The two bars were subsequently sintered at 950°C in an Ar atmosphere for 24 hours. Upon retrieval, some powder was scraped off of the sintered bar and its XRD pattern confirmed the bar was single phase $CuFeO_2$ (Fig. 17). The subsequent preparation steps were thus determined to be: prefiring in air at 835°C, heating in a N_2 atmosphere at 950°C, another step of heating at 950°C in a N_2 atmosphere and a final sintering step of heating at 950°C in an Ar atmosphere.

B.5.1.) Crystal $CuFeO_2$-A

Like before, because a previously grown single crystalline seed was not available for $CuFeO_2$, a small piece of approximately 7 mm length was cut from the 65 mm long sintered, polycrystalline $CuFeO_2$ bar, to be used as the seed rod. The remainder of the 65 mm $CuFeO_2$ bar, which was 6 mm in diameter, was used as the feed rod. The feed and the seed rod were placed in the NEC SC-N15HD optical image furnace, were both counter-rotated a rate of 25 rpm and put under an O_2 atmosphere. A floating zone was established between the rods by applying a voltage of 40.2 V to the halogen lamps. The feed and the seed rod were then synchronously lowered through the hot zone at a rate of 1.5 mm h^{-1}. In this way a large crystal of 35 mm length and 6 mm diameter was grown, showing some different small facets along

its growing axis. The $CuFeO_2$-A crystal is opaque black and believed to consist of several single crystalline domains.

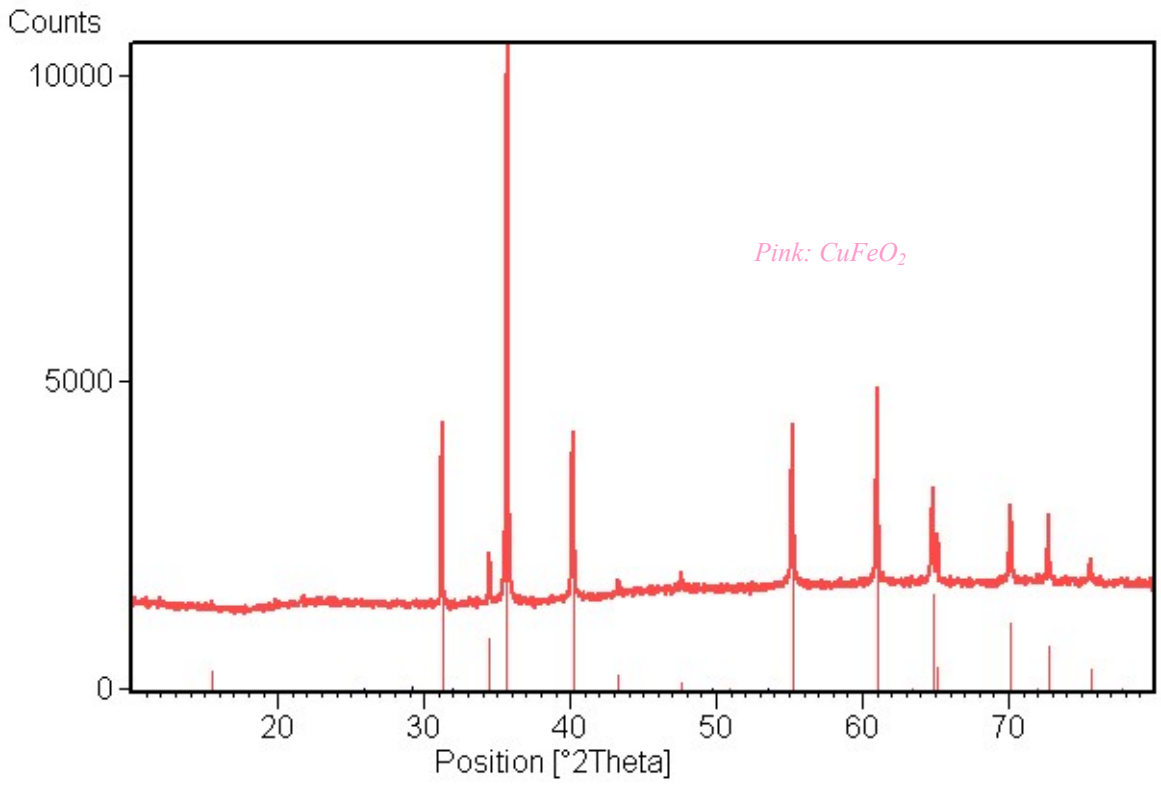

Fig. 17: *X -ray powder diffraction spectrum of the sintered powder, after the third heating treatment (in red).The pink coloured peaks represent the diffraction peaks of $CuFeO_2$, as reported in literature.*

B.5.2.) Crystal $CuFeO_2$-B

For the second growth, the same seed as in the first growth was used. As a feed rod, a 75 mm long, 6 mm diameter, sintered $CuFeO_2$ rod, previously synthesized at the LPCES, was used. The feed and the seed rod were placed in the NEC SC-N15HD optical image furnace, were both counter-rotated a rate of 25 rpm and put under an O_2 atmosphere. A floating zone was established between the rods by applying a voltage of 39.8 V to the halogen lamps. After the floating zone had been established the voltage was lowered to 38.0 V. The feed and the seed rod were then synchronously lowered through the hot zone at a rate of 1.5 mm h^{-1}. In this way a large single crystal of 60 mm length and 4 mm diameter was grown, showing 2 facets for a large part of its surface. The appearance of the crystal is reflective, opaque and black and the part of the crystal showing 2 facets is believed to be single crystalline.

B.6.) Further growth attempts

Next to the successful single crystal growth of the rare earth titanate family ($R_2Ti_2O_7$, where R = Tb, Gd, Ho and Dy) and $CuFeO_2$, also attempts have been made to grow single crystals of the other two compounds of interest here, $ZnCr_2O_4$ and $Y_2Mo_2O_7$, which were unsuccesful. The processes of synthesis and attempted single crystal growth of these two compounds are described in this section, along with the reason why single crystal growth fails for these

compounds. This section also illustrates nicely that single crystal growth using the floating zone technique is not as trivial as it may seem from the above paragraphs and that the process is strongly material dependent.

B.6.1.) Attempted growth of a zinc chromite ($ZnCr_2O_4$) single crystal

The spinel $ZnCr_2O_4$ was synthesized by the conventional solid-state reaction between the starting oxides:

$$ZnO + Cr_2O_3 \rightarrow ZnCr_2O_4$$

The first step of the synthesis was the thorough grinding and mixing of stoichiometric amounts of ZnO (Prolabo normapur, 99% pure, 10.4622 g) and Cr_2O_3 (Prolabo rectapur, 99% pure, 7.9682 g) and subsequently heating it for 16 hours at 1000°C in air. Next, the resulting powder was ground and isostatically pressed into two rods, both 10 mm in diameter and 90 and 65 mm in length, respectively. These rods were then heated for 30 hours at 1200°C in air to complete the reaction, after which they were thoroughly ground. The resulting powder was analyzed by powder XRD, which confirmed that the powder was $ZnCr_2O_4$ with no significant impurities (Fig. 18) . Finally, the powder was again isostatically pressed into 3 bars, all 7 mm in diameter and 20, 55 and 65 mm in length respectively. These bars were then sintered at 1400°C in air for 50 hours.

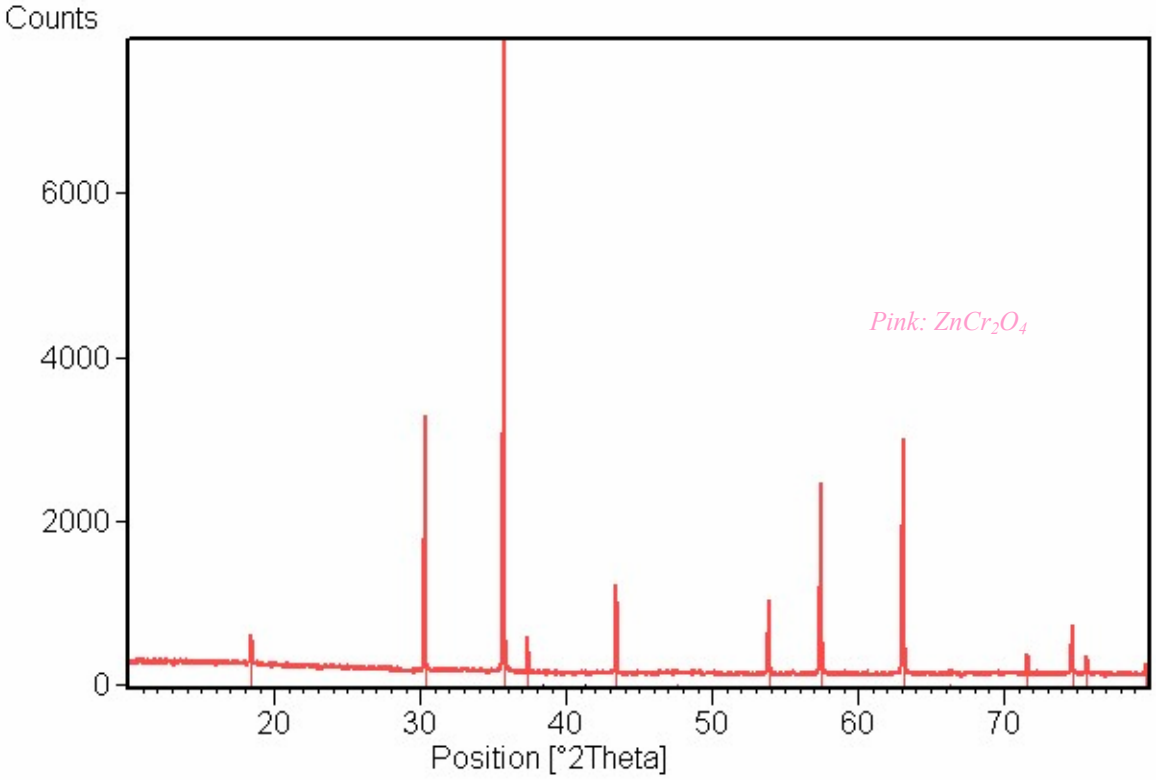

Fig. 18: *X -ray powder diffraction spectrum of the $ZnCr_2O_4$ powder, after the second heating treatment (in red).The pink coloured peaks represent the diffraction peaks of $CuFeO_2$, as reported in XRD references.*

Since there was no previously grown seed available for $ZnCr_2O_4$, the small sintered, polycrystalline bar of approximately 20 mm length was used as the seed rod. The 65 mm long sintered $ZnCr_2O_4$ bar was used as the feed rod. The feed and the seed rod were placed in the

NEC SC-N15HD optical image furnace were both counter-rotated a rate of 20-21 rpm and put under an O_2 atmosphere. Attempts were made to establish a floating zone between the feed and the seed rod. However, when applying a voltage of approximately 50 V to the halogen lamps, a large evaporation from both the feed and seed rod is observed, leaving a black residue on the rods' surfaces. This is most probably due to the compound starting to decompose into the starting oxides at the corresponding temperature. The reaction is the inverse of the synthesis: $ZnCr_2O_4 \rightarrow ZnO + Cr_2O_3$. ZnO is a very volatile compound which, after being formed in the assumed decomposition reaction, quickly evaporates from the hot zone. Powder XRD of the partially decomposed tips of the $ZnCr_2O_4$ bars shows the main constituents being $ZnCr_2O_4$ and Cr_2O_3, with a small trace of ZnO (Fig. 19). This agrees with the above interpretation of the reaction. Thus it is concluded that the growth of single $ZnCr_2O_4$ crystals is impossible using the floating zone technique, due to the instability of $ZnCr_2O_4$ at elevated temperature and the resulting decomposition reaction into the starting oxides. To grow zinc chromite single crystals one would have to use a technique which avoids heating $ZnCr_2O_4$ to high temperature (~1500°C).

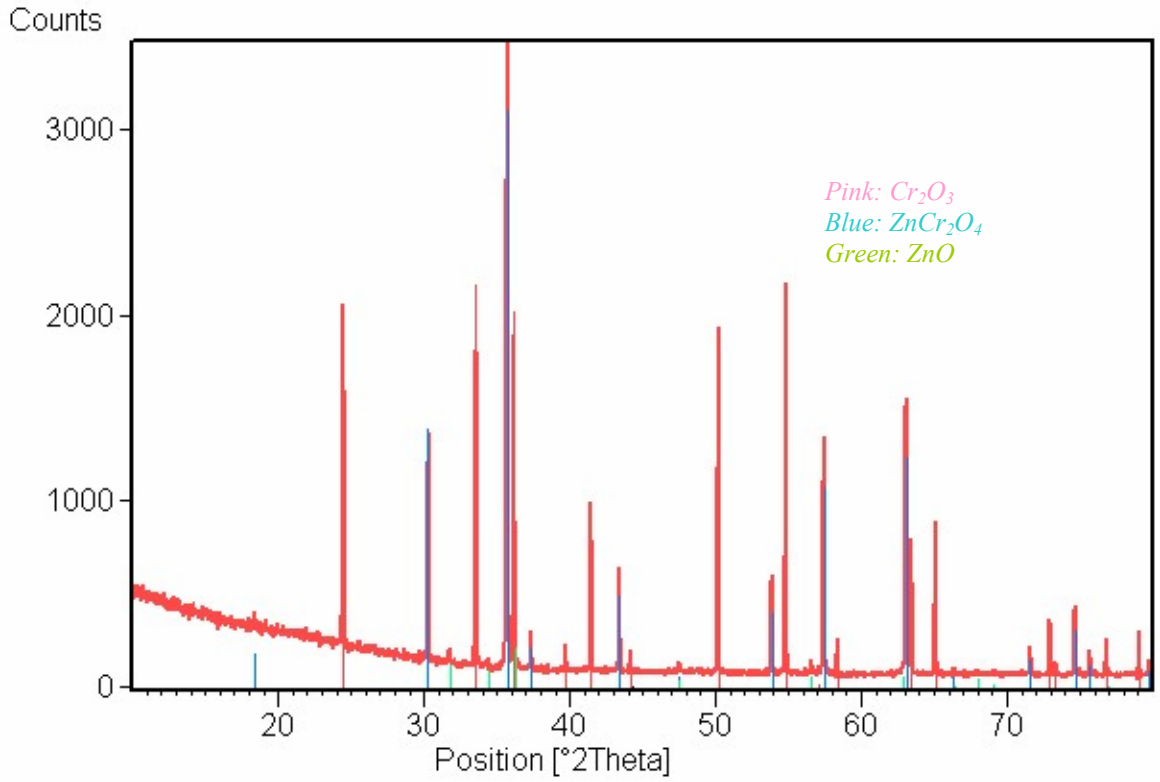

Fig. 19: *X -ray powder diffraction spectrum of the (partially) decomposed $ZnCr_2O_4$ powder, that was scraped from the feed and seed rod tips (in red). The coloured peaks are the measured diffraction peaks from references, where the different colours represent the different compounds in the powder. It clear that the main constituents are Cr_2O_3 and undecomposed $ZnCr_2O_4$, with a trace of ZnO.*

B.6.1.) Attempted growth of an yttrium molybdate ($Y_2Mo_2O_7$) single crystal

Initially, the $Y_2Mo_2O_7$ was synthesized in polycrystalline form using the familiar solid state reaction between the starting oxides:

$$Y_2O_3 + 2\,MoO_2 \rightarrow Y_2Mo_2O_7$$

The first step of the synthesis was the thorough grinding and mixing of stoichiometric amounts of Y_2O_3 (Rare Earth Products Ltd., 99.9% pure, 7.0318 g) and MoO_2 (Alfa Aesar, 99 % pure, 7.9682 g) and the subsequently firing of the mixture for 24 hours at 950 °C in an atmosphere of Ar gas. Next, the resulting powder was ground and isostatically pressed into a rod, 10 mm in diameter and 80 mm in length, respectively. The rod was then heated in an Ar atmosphere at 1250°C for 24 hours to complete the reaction, after which it was ground into a powder and this powder was isostatically pressed into a new rod, 6 mm in diameter and approximately 85 mm in length. This rod was subsequently sintered at 1300 °C for 30 hours, again in an Ar atmosphere.

Since there was no previously grown seed available for $Y_2Mo_2O_7$, a small piece of approximately 9 mm length was cut from the 85 mm long sintered, polycrystalline $Y_2Mo_2O_7$, to be used as the seed rod. The remainder of the 85 mm $Y_2Mo_2O_7$ bar, which was 6 mm in diameter, was used as the feed rod. The feed and the seed rod were placed in the NEC SC-N15HD image furnace, were both counter-rotated a rate of 22-25 rpm and put under an Ar atmosphere. Attempts were made to establish a floating zone between the feed and the seed rod. The limit voltages were applied to the halogen lamps and the rods were kept in this 'hottest possible zone' for over two hours, after which they were removed from the furnace, since no sign of melting had occurred. Then they were mounted in the CSI FZ-T-4000-H-II-P P image furnace, were counter-rotated and put under an Ar atmosphere, after which again the limit voltages were applied to the lamps (4 lamps in this case). Unfortunately, there was again no sign of melting of the compound, at the highest temperature of about 2100°C. The single crystal growth of $Y_2Mo_2O_7$ thus failed, most probably because its melting temperature could not be reached in the hot zone of the available furnaces. (Its melting temperature is estimated to be around 2400-2500 °C). Of course, this does not mean single crystal growth of $Y_2Mo_2O_7$ is impossible using this technique, the most advanced image furnaces to date can reach hot zone temperatures of ~2800°C, making reaching the melting point of $Y_2Mo_2O_7$ possible.

C.) Results & Discussion

C.1.) Magnetic susceptibility measurements of the rare earth titanates

The magnetic susceptibilities of the rare earth titanates were measured at the 'Laboratoire de Physico-Chimie de l'Etat Solide' (LPCES), using their Quantum Design MPMS-5 SQUID magnetometer.

C.1.1.) Magnetic susceptibility of terbium titanate ($Tb_2Ti_2O_7$)

To perform a measurement of the magnetic susceptibility of $Tb_2Ti_2O_7$, a small disc of 3 mm diameter and ~1 mm thickness was cut from the $Tb_2Ti_2O_7$-A crystal (its growth is described in section B.1.1) using a low speed diamond saw. This sample was mounted in the SQUID magnetometer of the LPCES. Subsequently, the magnetic susceptibility (defined as the ratio of the magnetization of the sample to the magnetic field) of the sample was measured in a 0.01 T applied magnetic field. Figure 20 shows a plot of the inverse susceptibility versus temperature.

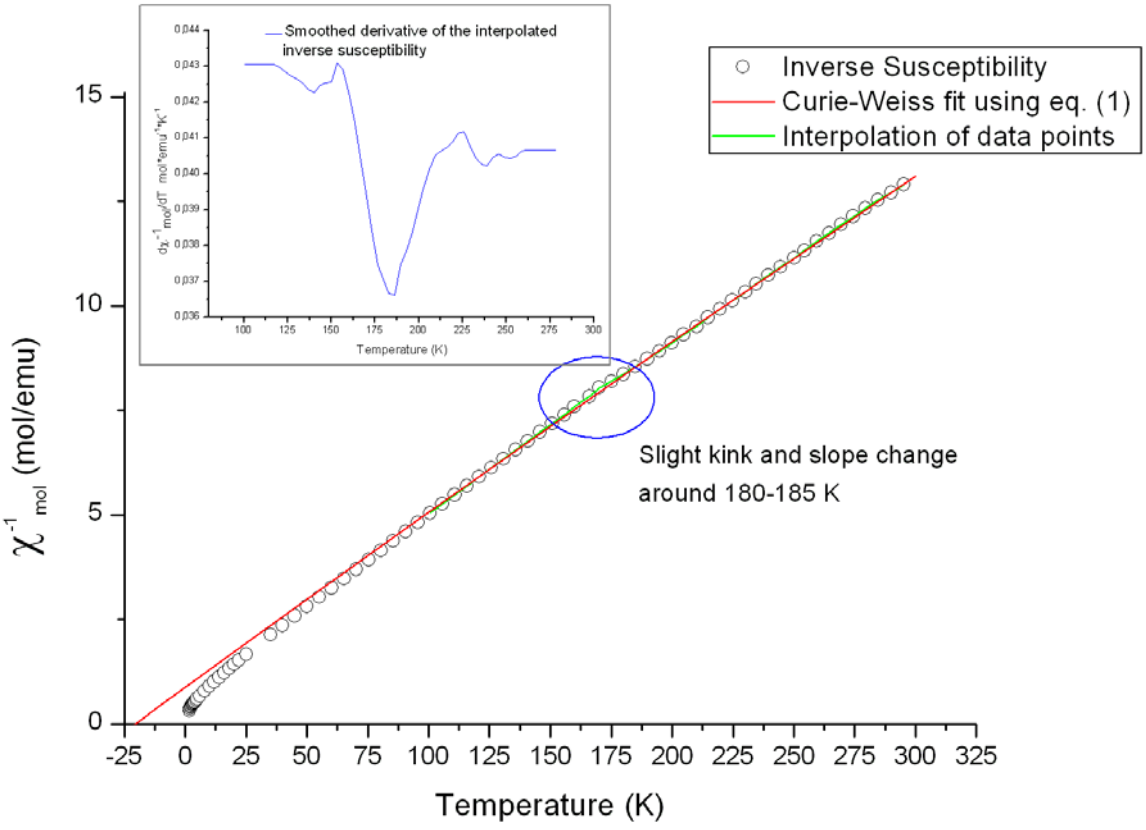

Fig. 20: *Temperature dependence of the inverse susceptibility of $Tb_2Ti_2O_7$. The red line is a fit of the high temperature data (100 K and up) to a Curie-Weiss form with a Van Vleck contribution (see text). The inset shows the smoothed derivative (blue line) of the curve that was interpolated from the data points (green line), where the slight kink (see text) of the inverse susceptibility is more easily seen.*

The inverse susceptibility plot was analysed by assuming for the susceptibility of a antiferromagnet in the paramagnetic regime:

$$\text{(CGS)}\quad \chi = \frac{2C}{T+\theta} + B\,, \qquad (1)$$

where C is the Curie constant in CGS units ($C = N\mu^2\mu_B^2 / 3k_b \cong \mu^2/8$), θ is the Curie-Weiss temperature (positive for an antiferromagnet) and B is a temperature independent Van Vleck contribution to the susceptibility. The measured susceptibility of fig. 20 shows a deviation from this behaviour below 100 K. This model was fitted to the high temperature experimental data (100 K and up) and a linear regression analysis of χ^{-1}_{mol} yields θ = 20.4 ± 1.6 K and μ = 9.66(8) μ_B. The temperature independent Van Vleck term (B) is determined to be 3.4(8) x 10^{-3} emu/mol. The large positive Curie-Weiss temperature (θ) indicates antiferromagnetic exchange coupling. The obtained values are in agreement with the values obtained by Gardner *et al.*, who reported $\theta \sim 19$ K and $\mu = 9.4\ \mu_B$ and with those reported by Gingras *et al.*, $\theta =$ 19 K and $\mu = 9.6\ \mu_B$. The paramagnetic moment obtained is also consistent with the free ion value of Tb^{3+} ($^7F_6$), $\mu = 9.72\ \mu_B$. Upon closer examination of the inverse susceptibility curve, a slight kink around 180-185 K is observed. To make the feature more obvious, an interpolation of the susceptibility data points was done (of the 100 K and up data), after which the resulting curve was smoothed. Then the derivative of this smoothed interpolation curve was calculated and smoothed again. The resulting derivative-curve is depicted in the inset of fig. 20, where this feature is more evident.

C.1.2.) Magnetic susceptibility of gadolinium titanate ($Gd_2Ti_2O_7$)

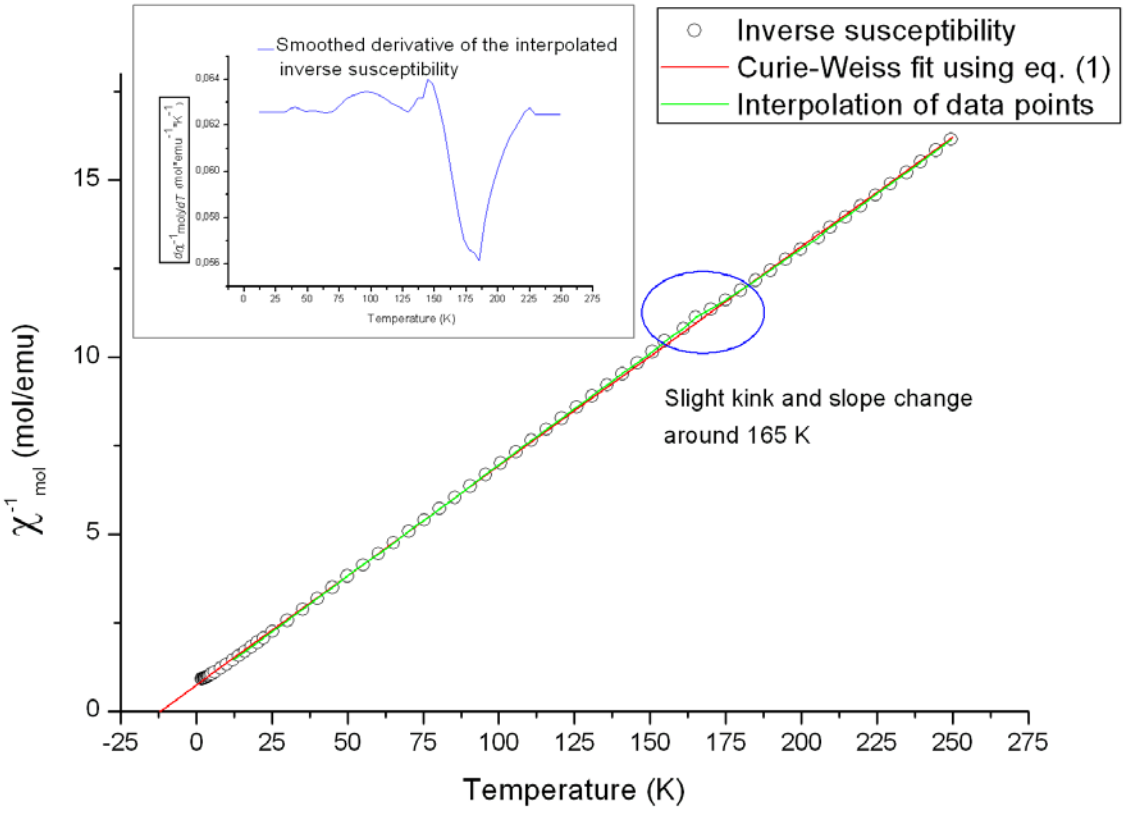

Fig. 21: *Temperature dependence of the inverse susceptibility of $Gd_2Ti_2O_7$. The red line is a fit of the higher temperature data (12 K and up) to a Curie-Weiss form (see text).*

For the measurement of the magnetic susceptibility of $Gd_2Ti_2O_7$, a small disc of 3 mm diameter and about ~1 mm thickness was cut from the $Gd_2Ti_2O_7$-A crystal (growth described in section B.2.1.) using a low speed diamond saw. The sample was mounted in the SQUID

magnetometer of the LPCES and subsequently, the magnetic susceptibility (the ratio of the magnetization of the sample to the magnetic field) of the sample was measured in a 0.01 T applied magnetic field. Figure 21 shows a plot of the inverse susceptibility versus temperature. The inverse susceptibility plot was analysed by using eq. (1), without a Van Vleck contribution (B = 0), since the Gd^{3+}-ion is not expected to have low-lying magnetic levels (L = 0). The measured susceptibility of fig. 21 shows a deviation from the Curie-Weiss behaviour below approximately 12 K. The model was fitted to the high temperature experimental data (12 K and up) and a linear regression analysis of χ^{-1} yields θ = 11.9(3) K and μ = 8.03(1) μ_B. The positive Curie-Weiss temperature(θ) indicates antiferromagnetic exchange coupling. The obtained values are consistent with the values reported by Cashion *et al.*[57], who reported θ = 11.7 K and μ = 7.8 μ_B, and Raju *et al.,* who reported θ = 9.6 K and μ = 7.7 μ_B. The paramagnetic moment obtained is also in agreement with the free ion value of Gd^{3+} ($^8S_{7/2}$), which is μ = 7.94 μ_B. As in the case of $Tb_2Ti_2O_7$, upon closer examination of the inverse susceptibility curve, a slight kink/bump is observed, around 165 K. To make the feature more obvious, an interpolation of the susceptibility data points was done (of the 12 K and up data), after which the resulting curve was smoothed. Then the derivative of this smoothed interpolation curve was calculated and smoothed again. The resulting derivative-curve is depicted in the inset of fig. 21, where this feature is more pronounced.

C.1.3.) Magnetic susceptibility of holmium titanate ($Ho_2Ti_2O_7$)

To perform a measurement of the magnetic susceptibility of holmium titanate, a small disc of 4 mm diameter and about 1.5 mm thickness was cut from the $Ho_2Ti_2O_7$-B crystal (growth described in section B.3.2) using a low speed diamond saw. This sample was mounted in the SQUID magnetometer of the LPCES and subsequently, the magnetic susceptibility of the sample was measured in a 0.01 T applied magnetic field. Figure 22 shows a plot of the inverse susceptibility versus temperature. The inverse susceptibility plot was analysed by assuming (for a ferromagnet in the paramagnetic regime):

$$\text{(CGS) } \chi = \frac{C}{T+\varphi} + B, \qquad (2)$$

where B is a Van Vleck contribution to the susceptibility and φ is the Curie-Weiss temperature (negative for a ferromagnet). This model was fitted to the higher temperature experimental data (6 K and up) and a linear regression analysis of χ^{-1} yields φ = - 2.2(8) K, which is consistent with the value reported by Bramwell *et al.*[58] (-1.9K). This small, negative value (note the definition in eq.(2)) for φ initially led to the assumption of weak *ferro*magnetic exchange interactions between nearest neighbour Ho^{3+}-ions[21,21], as mentioned in the introduction (section A.2.1.). Since free Ho^{3+}-ions have a large magnetic moment though, μ = 10.607 μ_B ($^5I_8$ ground state), the dipolar interactions between neighbouring Ho^{3+}-ions play an important role in the effective nearest neighbour (n.n.) interactions as well. As mentioned in section A.2.1., it turns out the n.n. exchange interactions are in fact antiferromagnetic, while the dominant dipolar n.n. interactions are of ferromagnetic nature. Consequently, the effective n.n. interactions are slightly *ferro*magnetic, explaining the negative φ-value. Another consequence of the dipolar interactions being dominant is the fact that extracting the real value of μ from the inverse susceptibility curve becomes highly non-trivial, since more elaborate models taking the dipolar interaction into account are needed. As in the previous rare earth titanates, upon closer examination of the inverse susceptibility curve, a slight kink/bump is observed, around 170 K for $Ho_2Ti_2O_7$. To make the feature more obvious, an interpolation of the susceptibility data points was done (of the 6 K and up data), after which

the resulting curve was smoothed. The derivative of this smoothed interpolation curve was calculated and is depicted in the inset of fig. 22. where this feature is more evident.

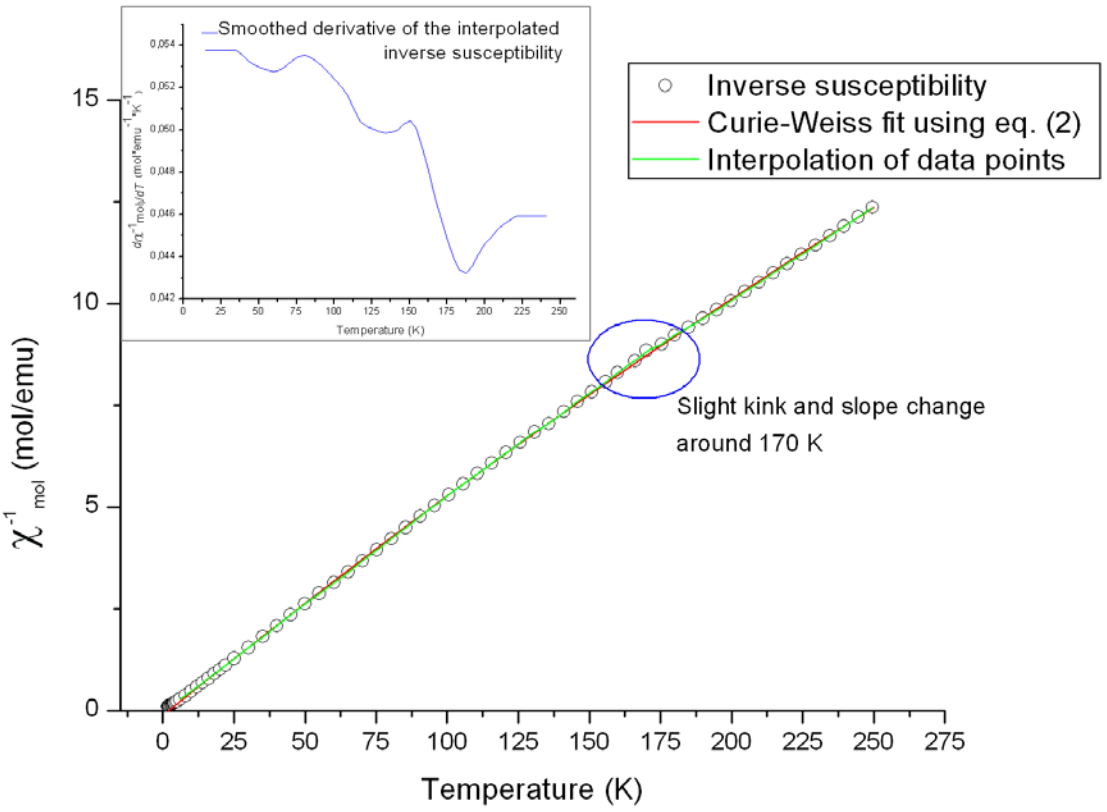

Fig. 22: *Temperature dependence of the inverse susceptibility of $Ho_2Ti_2O_7$. The red line is a fit of the higher temperature data (6 K and up) to a Curie-Weiss form with a Van Vleck contribution (see text above).*

C.1.4.) Magnetic susceptibility of dysprosium titanate ($Dy_2Ti_2O_7$)

Again, in order to perform a measurement of the magnetic susceptibility, a low speed diamond saw was used to cut a small disc of 3 mm diameter and about 2 mm thickness from the $Dy_2Ti_2O_7$-B crystal (growth described in section B.4.2). This sample was mounted in the SQUID magnetometer of the LPCES and subsequently, the magnetic susceptibility (magnetization of the sample divided by the magnetic field) of the sample was measured in a 0.01 T applied magnetic field. Figure 23 shows a plot of the inverse susceptibility versus temperature. The inverse susceptibility plot was analysed using equation (2). This model was fitted to the higher temperature experimental data (10 K and up) and a linear regression analysis of χ^{-1} yields φ = - 0.95 ± 0.14 K, which is consistent with the value reported by Bramwell *et al.* (~ -1K). As in the case of $Ho_2Ti_2O_7$, this small, negative value for φ initially led to the assumption of weak *ferro*magnetic exchange interactions between nearest neighbour Dy^{3+}-ions. Since free Dy^{3+}-ions also have a large magnetic moment (μ = 10.646 μ_B ($^6H_{15/2}$ ground state), the dipolar interactions between neighbouring Dy^{3+}-ions are dominant in $Dy_2Ti_2O_7$ as well. As mentioned in section A.2.1., it turns out the n.n. exchange interactions are in fact antiferromagnetic, while the dominant dipolar n.n. interactions are of ferromagnetic nature. Consequently, just like in $Ho_2Ti_2O_7$ the effective n.n. interactions are slightly *ferro*magnetic, explaining the negative φ-value. Also for dysprosium titanate extracting the real value of μ from the inverse susceptibility curve becomes highly non-trivial, since more

elaborate models taking the dipolar interaction into account are needed. As in the previous rare earth titanates, upon closer examination of the inverse susceptibility curve, a slight kink/bump is observed, around 170 K for $Ho_2Ti_2O_7$. To make the feature more obvious, an interpolation of the susceptibility data points was done (of the 6 K and up data), after which the resulting curve was smoothed. The derivative of this smoothed interpolation curve was calculated and is depicted in the inset of fig. 23. where this feature is more evident.

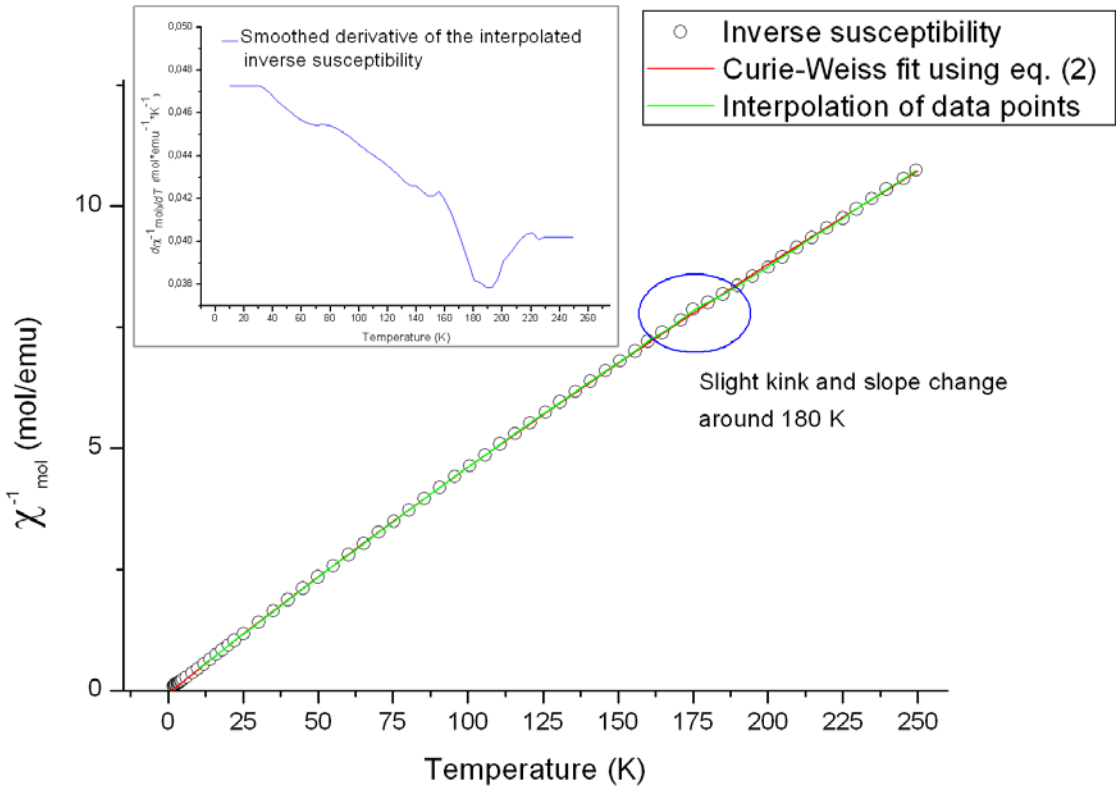

Fig. 23: *Temperature dependence of the inverse susceptibility of $Dy_2Ti_2O_7$. The red line is a fit of the higher temperature data (10 K and up) to a Curie-Weiss form with a Van Vleck contribution (see text).*

The occurrence of a slight bump and/or kink in the inverse susceptibility of all of the rare earth titanates is quite striking. These features have previously been observed and interpreted as a negative curvature of χ^{-1} at high temperatures, and thus ascribed to a temperature independent Van Vleck susceptibility, which was also initially done here. Upon close examination, however, the Curie-Weiss fits with including Van Vleck term, although accounting for a slight negative curvature at higher temperatures, do not reproduce the bumps observed in these data. The bump features may have been previously overlooked because of lack of data points in the corresponding temperature range. The fact that these features occur in all the rare earth variants of $R_2Ti_2O_7$ investigated here however, combined with the fact that they occur at slightly different temperatures for different R, indicates these features are related to the $R_2Ti_2O_7$ pyrochlore structure, rather than simply being a measuring artefact. The magnetic excited states which are the origin of the Van Vleck term in the susceptibility are expected to be the low lying crystal field levels of the respective R^{3+}-ions. This because when examining the derivatives of the magnetic susceptibilities of the rare earth titanates (insets in fig. 20-23), it becomes clear that next to the main feature (dip around ~175 K) in all of the $R_2Ti_2O_7$ variants, a second, continuous negative slope change is observed for the Ho and Dy variants and an seemingly abrupt slope change is observed for the Tb variant. This is

interpreted as a consequence of the presence of a Van Vleck term in the susceptibility. Considering that this second feature is not present in the Gd variant (here the slope above and below the dip is the same, inset fig. 21), combined with the fact that the Gd^{3+}-ion is not expected to have low lying crystal field levels ($L = 0$) while for the other variants this is expected, the Van Vleck terms in the Tb, Ho and Dy variants are ascribed to low lying crystal field excitations. For the Tb variant, the derivative of the inverse molar susceptibility (inset of fig. 20) apparently shows an abrupt change of slope across the phase transition, whereas a continuous slope change is expected. This could be explained by a fitting artifact, since the two 'bumps' on either side of the phase transition dip in the derivative of χ^{-1}_{mol} and the fact that the derivate was only determined down to 100 K, might mask the continuity of this slope change. It should be noted though, that the error in determining the Van Vleck terms is quite large (estimated to be about 50 % of the values), meaning the quality of the fits is not very dependent on the specific value of the Van Vleck term. Overall, these findings are the first indication of something happening at temperatures of around ~175 K in the rare earth titanates' (magnetic) structure.

C.2.) Preparation of Raman samples: X-ray Laue diffraction and sample polishing

Prior to performing polarization controlled, inelastic light scattering experiments, the orientation of the single crystals needs to be determined. This was done using Laue X-ray diffraction, on the Philips PW 1710 diffractometer of the MSC^{+}, which is equipped with the Polariod XR-7 system. Due to time constraints, only two crystals have been investigated using Raman spectroscopy, and thus only these two have been oriented and polished. The first of these crystals is the crystal $Tb_2Ti_2O_7$-A (fig. 10.a., growth described in section B.1.1). First, a Laue photograph was taken with the incoming X-ray beam perpendicular to one of the natural facets on the side of the $Tb_2Ti_2O_7$-A (fig. 24). Simulation of the expected diffraction pattern of $Tb_2Ti_2O_7$ (cubic space group Fd-3m, lattice constant 10.15 Å) confirmed this facet is the [111] plane of the crystal.
Next, it was calculated how to rotate the crystal to have the incident X-ray beam perpendicular to one of the <100> planes of the crystal. The crystal was rotated into this orientation and a small slice of about 1.3 mm thick was cut from the crystal using a low speed diamond saw, in a way the surfaces of this slice would be one of the <100> planes of the structure. To check whether the surface of the slice was indeed one of the equivalent <100> planes of the crystal, another Laue photograph was taken (fig. 25), which indeed confirmed the surface to be a <100> plane.

The second crystal that was oriented is the $Gd_2Ti_2O_7$-A crystal (growth described in section B.2.1.). Also for this crystal, a Laue picture of one of its natural facets showed this to be one of the <111> directions. Rotation of the crystal and subsequent cutting of a thin slice (about 1.4 mm), with its surfaces being one of the <100> planes (confirmed by a Laue photograph) completed the orientation of the $Gd_2Ti_2O_7$-A crystal in a way, very similar to the orientation procedure of the $Tb_2Ti_2O_7$-A crystal.

Before the sample slices could be used in Raman experiments, their rough surfaces had to be smoothed. This is necessary because when working in 180° backscattering geometry, a rough surface causes quite a substantial amount of elastic backscattering, making it impossible to resolve features in the region close to the Rayleigh scattering (at low wavenumbers). Since one of the aims of this work is the measurement of this 'low wavenumber region', smoothing of the surfaces of the sample slices is needed. This smoothing is done by mounting the sample slice on the sample holder of a polishing tool. Hereafter, Laue X-ray diffraction is used to make sure the crystal plane that will be polished is indeed the one that is intended to be polished (one of the <100> planes for both $Tb_2Ti_2O_7$ and

$Gd_2Ti_2O_7$). The polishing tool is equipped with an angular correction mechanism, making it possible to correct for a mismatch of the exposed crystal plane and the crystal plane intended to be polished. Small mismatches, which are often caused by mounting the sample on the sample holder of the polishing tool, can be corrected up to an angular difference of 5°, with a precision of $^5/_{72} \approx 6.9 * 10^{-2}$ °.

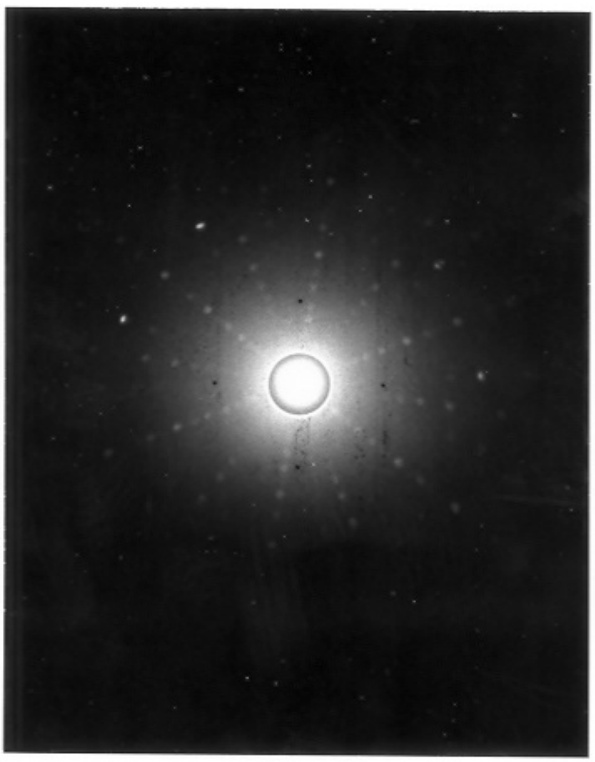

Fig. 24: *X-ray Laue photograph of the $Tb_2Ti_2O_7$-A crystal. The incoming beam is perpendicular to one of the natural faces of the crystal. The threefold rotation axis indicates that the natural facet is one of the <111> planes of the crystal.*

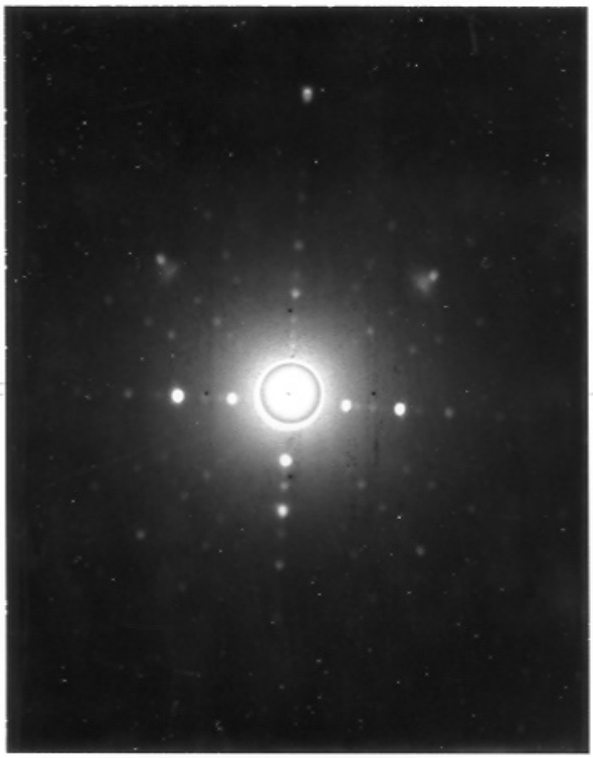

Fig. 25: *Laue photograph of the $Tb_2Ti_2O_7$ sample slice. The fourfold rotation axis is evident in this picture, confirming the surface of the slice to be one of the <100> planes of $Tb_2Ti_2O_7$.*

After the crystal is oriented on the polishing tool correctly, the exposed crystal plane is smoothed by grinding the polishing tool, and thus the rough surface of the sample slice, on sandpaper of a certain roughness. This grinding is done with paraffin oil functioning as a lubricant. To effectively polish the sample, the sample is successively polished using grinding paper of decreasing coarseness. The grinding papers that were used were, in this order, Struers Silicon-Carbide (SiC) paper, roughness grit 220, then Struers SiC paper grit 320, grit 500, 800, 1000, 1200, 2400 and grit 4000, followed by Buehler ultra-prep diamond lapping film polishing discs (type A continuous) of roughness 3 micron and 1 micron. All the polishing was done by making 8-type movements with the polishing tool, pushing it ever so slightly against the grinding paper by applying very light downward pressure to the polishing tool. The polishing was done with the sandpaper placed on a very thoroughly cleaned, smooth glass plate, the Buehler polishing discs were also glued to such a glass plate. The procedure of polishing is to change to a grinding paper that is less rough only after the sample surface has the same roughness as the current grinding paper. Going down the list of grinding papers of

decreasing coarseness this way, while carefully cleaning the polishing tool between every step, the surfaces (both sides) of the $Tb_2Ti_2O_7$ and $Gd_2Ti_2O_7$ sample slices were polished, untill they were completely reflective to the eye. After polishing again the orientation of the surfaces were checked and confirmed to be <100> planes, again using Laue X-ray diffraction.

C.3.) Raman spectroscopy

The mayor investigative tool that was used to probe the frustrated systems is Raman spectroscopy. Polarization controlled, inelastic light scattering experiments were performed on both the $Tb_2Ti_2O_7$ and $Gd_2Ti_2O_7$ samples. The experiments were performed in a 180° backscattering configuration, using a three-grating micro-Raman spectrometer (T64000-Jobin Yvon), consisting of a double grating monochromator (acting as a spectral filter) and a polychromator which disperses the scattered light onto a liquid nitrogen cooled CCD detector. The frequency resolution was better than 1 cm^{-1} for the frequency region considered. The triple grating configuration allows for the measurement of a broad spectrum from 9000 cm^{-1} down to 4 cm^{-1}. The samples were placed in a liquid helium cooled optical flow-cryostat (Oxford Instruments). The temperature was controlled with an accuracy of 0.1 K in the whole range of measured temperatures (from 2.5 to 295 K). The 532.6 nm light of a Nd:YVO_4 laser was used to excite the samples. The polarization was controlled both on the incoming and outgoing beam, giving access to all the linear polarization-combinations that can be probed in the back-scattering configuration.

C.3.1.) Raman spectroscopy of terbium titanate ($Tb_2Ti_2O_7$)

The polished sample slice of $Tb_2Ti_2O_7$ was mounted on a copper sample plate, which in turn was mounted on the cold finger of the flow cryostat. The sample was pumped to a vacuum pressure of ~10^{-7} bar. Once this pressure was reached, the room temperature (295 K) parallel polarization spectrum (porto notation c(bb)c, meaning both the polarization of the incoming light and that of the scattered light are parallel to the sample's b-axis) and the perpendicular polarization spectrum (c(ba)c, incoming light polarization // to b-axis, scattered light polarization // to a-axis) were measured (fig. 26).

Group theory analysis predicts that, for the cubic rare earth titanate structure of space group *Fd-3m*, each sublattice of the unit cell has the following irreducible representations:

16(c) (Ti^{4+}-sublattice) $= A_{2u} + E_u + 2F_{1u} + F_{2u}$
16(d) (R^{3+}-sublattice) $= A_{2u} + E_u + 2F_{1u} + F_{2u}$
48(f) (O(1)-sublattice) $= A_{1g} + E_g + 2F_{1g} + 3F_{2g} + A_{2u} + E_u + 3F_{1u} + 2F_{2u}$
8(a) (O(2)-sublattice) $= F_{1u} + F_{2g}$

This makes the total number of zone center normal modes 26:

$$\Gamma = A_{1g} + E_g + 2F_{1g} + 4F_{2g} + 3A_{2u} + 3E_u + 8F_{1u} + 4F_{2u}$$

Of these normal modes, only A_{1g}, E_g and $4F_{2g}$ are Raman active modes. The $8F_{1u}$ modes are infrared active and the remaining modes are optically inactive. The fact that all the Raman active modes come from the oxygen sublattices explains the fact that the room temperature spectra of the rare earth titanates are only slightly R-dependent. The assignment of the irreducible representations of the Raman active modes to the observed peaks in the Raman spectrum of $Tb_2Ti_2O_7$ is depicted in fig. 26. This assignment is based on comparison with assignments in other works[59,60,61] and on measurements of the angular dependence of the peak

intensities (where the angle between the incoming light polarization and the b-axis was varied from -45° to 45°).

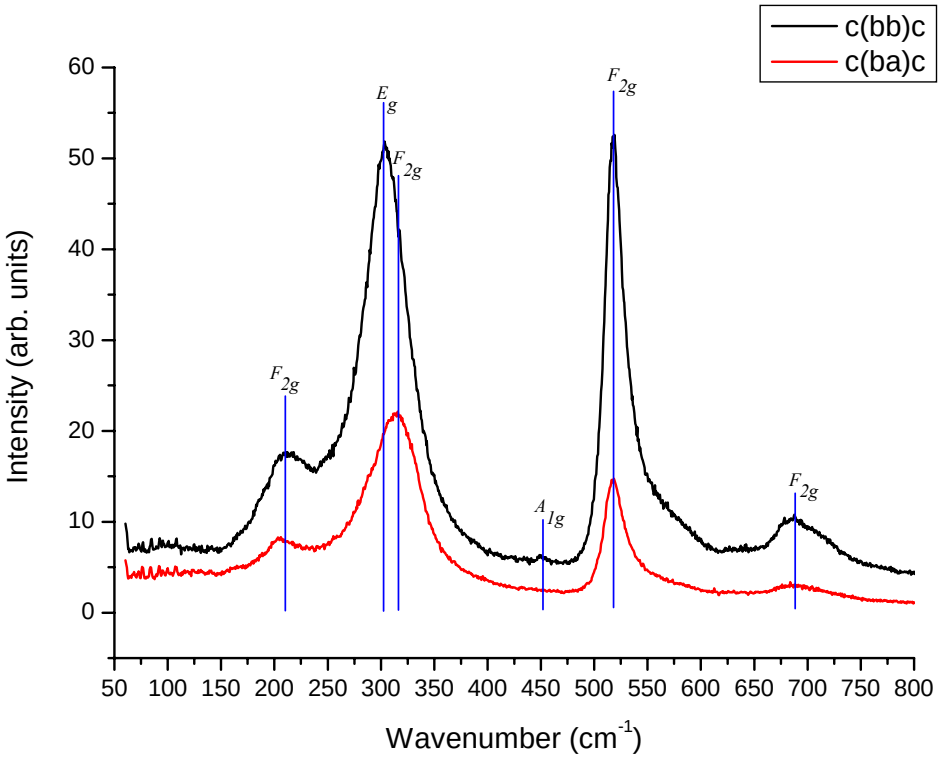

Fig. 26: *Room temperature Raman spectra of $Tb_2Ti_2O_7$ in both c(bb)c and c(ba)c configuration. Also, the assignment of the irreducible representations of the Raman active modes to the observed peaks is indicated.*

To illustrate how the assignment on the basis of this angular dependence of the peak intensities is done, an example is given here. If one defines e^i and e^s as the arbitrary unit vectors for the polarizations directions of the incident and scattered light, respectively, the scattering intensity is[62]:

$$\phi(k) \propto \left| \sum_{j,l} e_j^s \chi_{jl,k} e_l^i \right|^2 \qquad (3)$$

where j and l run over the Cartesian coordinates x, y and z of the Raman tensor χ of mode k. If a mode is degenerate, it is necessary to sum the intensities originating from the different Raman tensors corresponding to the same mode. In the case of $R_2Ti_2O_7$, the E_g and F_{2g} modes are doubly and triply degenerate, respectively. The Raman tensors of the different Raman active modes of $R_2Ti_2O_7$ are:

$$A_{1g}: \begin{pmatrix} a & 0 & 0 \\ 0 & a & 0 \\ 0 & 0 & a \end{pmatrix} \quad E_{g,1}: \begin{pmatrix} b & 0 & 0 \\ 0 & b & 0 \\ 0 & 0 & -2b \end{pmatrix} \quad E_{g,2}: \begin{pmatrix} -b\sqrt{3} & 0 & 0 \\ 0 & b\sqrt{3} & 0 \\ 0 & 0 & 0 \end{pmatrix} \quad F_{2g,1}: \begin{pmatrix} 0 & 0 & 0 \\ 0 & 0 & d \\ 0 & d & 0 \end{pmatrix} \quad F_{2g,2}: \begin{pmatrix} 0 & 0 & d \\ 0 & 0 & 0 \\ d & 0 & 0 \end{pmatrix} \quad F_{2g,3}: \begin{pmatrix} 0 & d & 0 \\ d & 0 & 0 \\ 0 & 0 & 0 \end{pmatrix}$$

Now, the polarization directions of the incident and scattered light (described in the coordinate system of the crystal) as a function of the angle θ between the crystal b-axis and the incoming polarization direction are:

For parallel polarization (c(bb)c) probing: $e^i = e^s = \begin{pmatrix} \cos\theta \\ \sin\theta \\ 0 \end{pmatrix}$

For perpendicular polarization (c(ba)c) probing: $e^i = \begin{pmatrix} \cos\theta \\ -\sin\theta \\ 0 \end{pmatrix}$; $e^s = \begin{pmatrix} \sin\theta \\ \cos\theta \\ 0 \end{pmatrix}$

This yields for the intensities of the A_{1g}, E_g and $4F_{2g}$ modes, using eq. (3):

Table 2

mode	Intensity in c(bb)c probing	Intensity in c(ba)c probing
A_{1g}	$\propto a^2$	$= 0$
E_g	$\propto (b^2 + 3b^2(\sin^2\theta - \cos^2\theta))$	$\propto 12b^2\cos^2\theta \sin^2\theta$
F_{2g}	$\propto 4d^2\cos^2\theta \sin^2\theta$	$\propto d^2(\cos^2\theta - \sin^2\theta)$

By comparing these theoretical θ-dependencies of the intensity to the experimentally determined θ-dependence of the observed Raman peaks, a peak assignment can be made. As an example, fig. 27 shows the experimentally determined (fitted) intensities of the ~304 cm^{-1} and ~317 cm^{-1} peaks as a function of θ and their theoretical dependencies (see table 2) for both the c(bb)c (fig. 26.a.) and the c(ba)c (fig. 26.b.) room temperature spectrum.

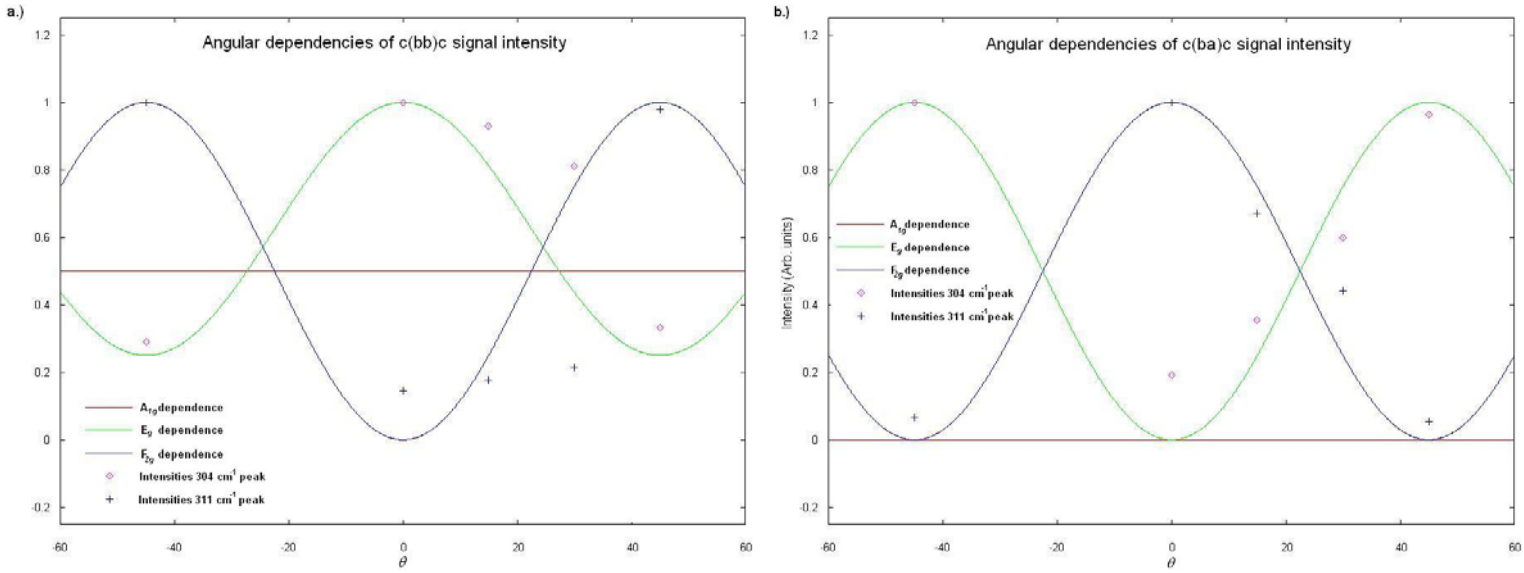

Fig. 27: *Angular dependence of peak intensities in both the c(bb)c (**a.**) and c(ba)c (**b.**) Raman spectra. The solid lines are the theoretically expected angular dependencies from table 2 and the data points show the experimentally determined intensities of the ~304 cm^{-1} and ~317 cm^{-1} peaks as a function of θ.*

When comparing the experimentally determined angular dependence with the theoretically calculated curves, it becomes clear that the angular dependence of the ~304 cm^{-1} mode follows the calculated curve for an E_g mode, while the angular dependence of the ~317 cm^{-1} mode follows the calculated curve for an F_{2g} mode. Therefore, on the basis of fig. 27, the ~304 cm^{-1} mode can be assigned to the E_g mode and the ~317 cm^{-1} signal can be assigned to one of the 4 F_{2g} modes. It can also be seen in fig. 27 that the A_{1g} mode is only expected in the c(bb)c spectrum (compare red curves in fig. 27 a. and b.). The only mode in fig. 26 that fulfills this condition is the 450 cm^{-1} mode, meaning this signal can be assigned to the A_{1g} mode. It should be noted that, some of assigned F_{2g} modes do show the wavelike angular expected, but with a large, constant background peak intensity. Although this background intensity cannot currently be explained, the assignment is maintained, since the Laue X-ray diffraction patterns show no sign of polycrystals or mis-alignment of the incoming laser beam from the sample c-axis (which might explain a background intensity).

As the next step in the Raman investigation of $Tb_2Ti_2O_7$, the full temperature dependence of both the parallel polarization spectrum (porto notation c(bb)c) and the perpendicular polarization spectrum (c(ba)c) was measured. This was done by subsequently bringing the sample into thermal equilibrium with the cooling helium flow at the desired measuring temperatures (ranging from 295 to 2.5 K). Fig. 28 shows the full temperature dependence of the c(bb)c spectrum of $Tb_2Ti_2O_7$.

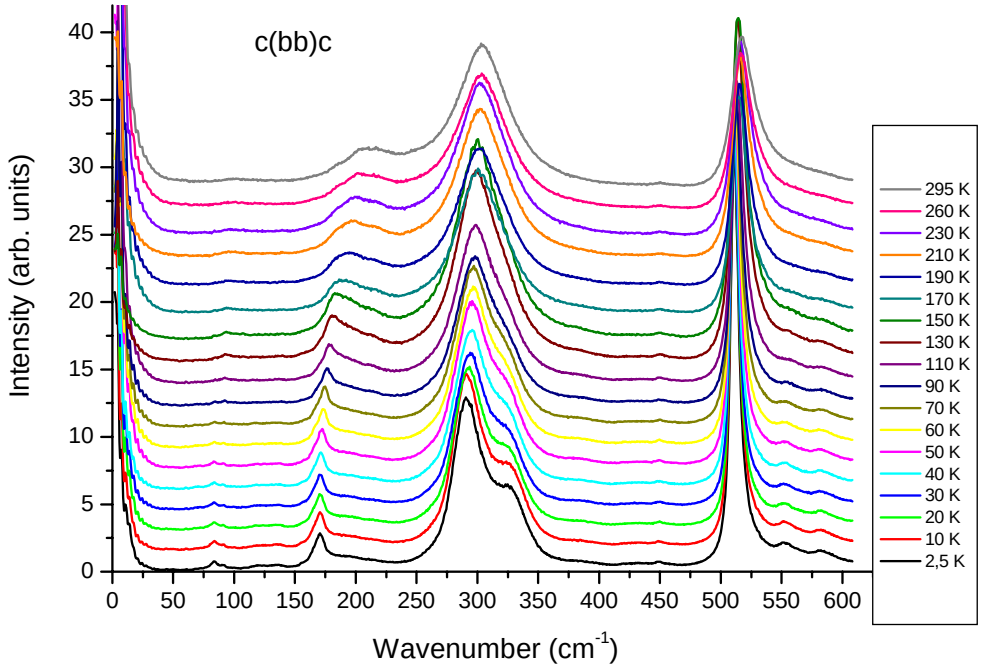

Fig. 28: *Temperature dependence of the c(bb)c Raman spectrum. The spectrum shows several changes between the temperatures 190 K and 150 K.*

What is observed in the temperature dependence of the c(bb)c spectrum of $Tb_2Ti_2O_7$ (more clearly seen in fig. 29 and fig. 30) are several changes when comparing the spectra measured at 190 and 150 K (note that this is across the temperature range where the magnetic

susceptibility also shows a feature, fig. 20). There is the shape change/frequency shift of the ~205 cm^{-1} F_{2g} mode, the frequency shifts of the ~304 cm^{-1} E_g and the ~ 317 cm^{-1} F_{2g} modes (making them more distinguishable), the appearance of some new modes around ~83, ~90, ~170, ~555 and ~580 cm^{-1} (see fig. 29) and the frequency shift and sharpening of the ~515 cm^{-1} F_{2g} mode (see fig. 30). These changes are the second hint towards something happening to the pyrochlore structure around 180-185 K

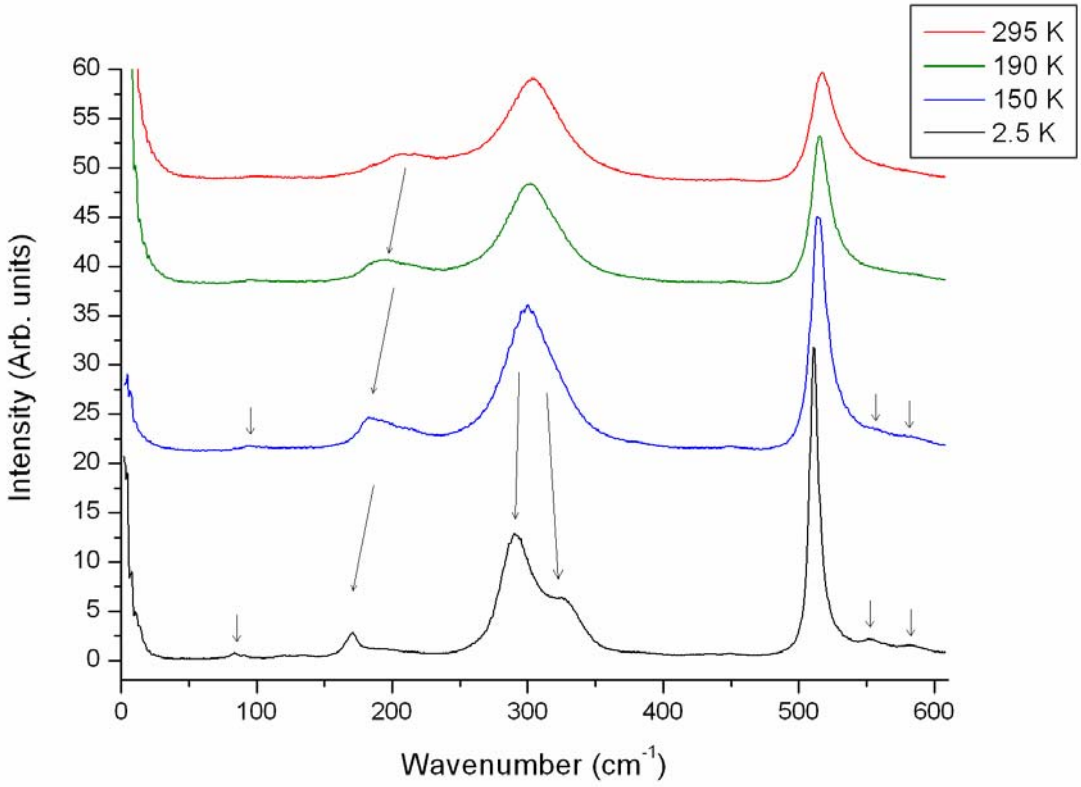

Fig. 29: *Temperature dependence of the c(bb)c Raman spectrum. The changes between 190 K and 150 K are described in the text and where possible, indicated by arrows.*

The most compelling evidence for a possible phase transition around 180-185 K in $Tb_2Ti_2O_7$, however, comes from the temperature dependence of the c(ba)c spectrum of $Tb_2Ti_2O_7$, which is depicted in figure 31. As in the c(bb)c spectrum, several changes are observed when comparing the 190 K and the 150 K spectrum. The shape change/frequency shift of the ~205 cm^{-1} F_{2g} mode, the frequency shifts of the ~304 cm^{-1} E_g and the ~ 317 cm^{-1} F_{2g} modes (which make them more distinguishable), the frequency shift and sharpening of the ~515 cm^{-1} F_{2g} mode and the appearance of the ~170 cm^{-1} mode are also observed in the c(ba)c spectrum, as can be seen in fig 31.

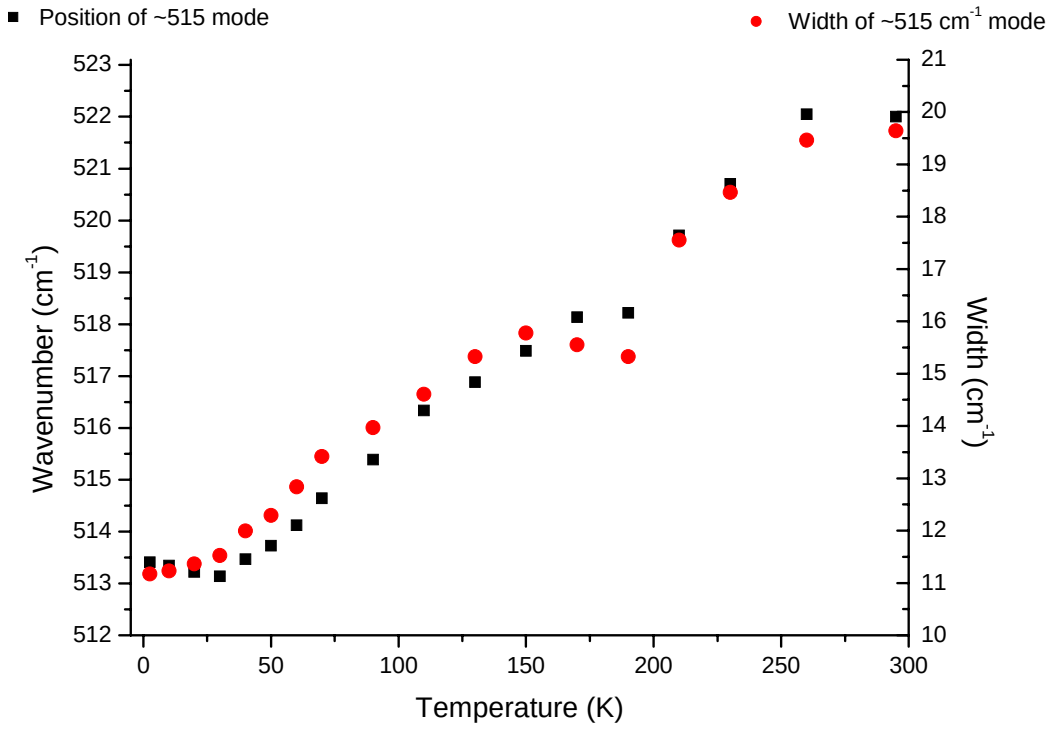

Fig. 30: *Temperature dependence of the position (black squares, left y-axis) and the width (red circles, right y-axis) of the ~515 cm^{-1} mode in the c(bb)c spectrum of $Tb_2Ti_2O_7$.*

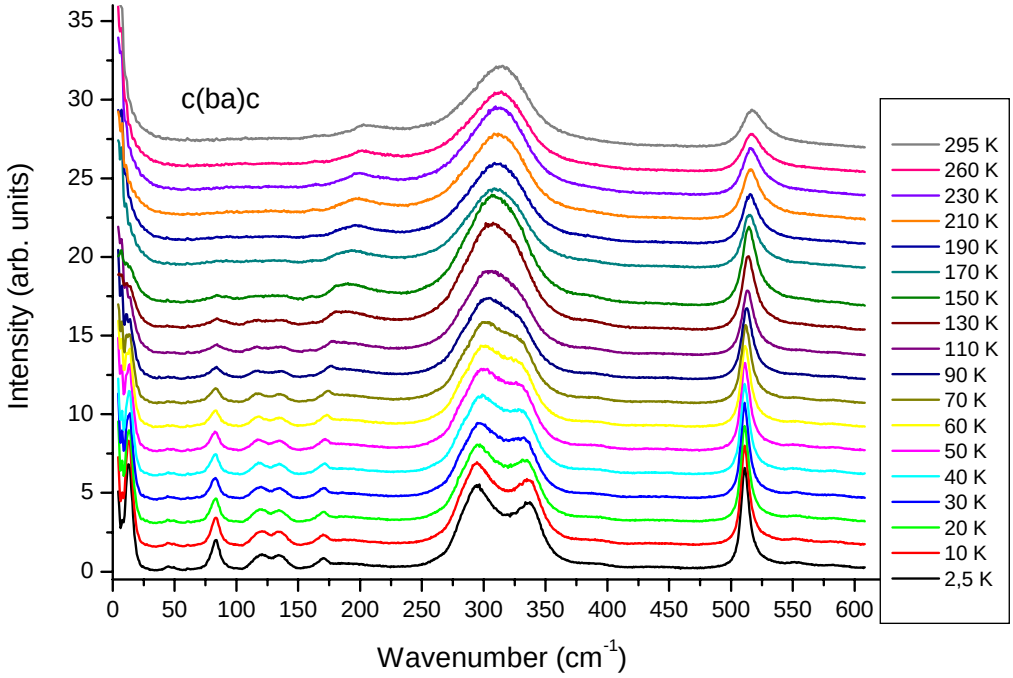

Fig. 31: *Temperature dependence of the c(ba)c Raman spectrum of $Tb_2Ti_2O_7$. The spectrum shows several changes between the temperatures ~190 K and 150 K.*

In addition, several excitations at lower wavenumbers are observed at temperatures below 190 K. The appearance of two modes around round ~83 and ~90 is not observed, most probably since they are not resolved against the strong background of one of these low-lying excitations (they are observed in the $Gd_2Ti_2O_7$ c(ba)c spectrum). The low-lying excitations are ascribed to Tb^{3+}-ion crystal field excitations. Crystal field calculations for the Tb^{3+}ion in $Tb_2Ti_2O_7$, partially confirmed by inelastic neutron scattering[10,63,64], lead to the following energy level scheme for the lowest crystal field levels (fig. 32).

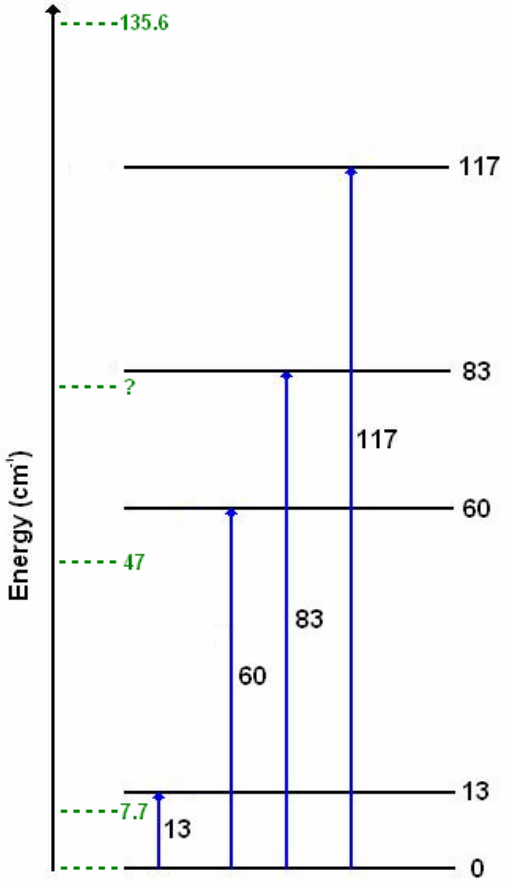

Fig. 32: *The energy level scheme of the Tb^{3+}ion in $Tb_2Ti_2O_7$, based on the crystal field calculations from ref. 9. The blue arrows show the excitations observed in the c(ba)c Raman spectrum of $Tb_2Ti_2O_7$ (see fig. 33).*

As can be seen in fig. 33, which is a zoom-in on the low-wavenumber region of the 2.5 K spectrum of fig. 31, the crystal field levels and possible excitations (the blue arrows in fig. 32) correspond almost exactly to the low-lying excitations observed in the c(ba)c Raman spectrum of $Tb_2Ti_2O_7$ below ~190K. The excitations from the crystal field ground state to the higher crystal field levels, of calculated values 13, 60, 83 and 117 cm^{-1}, are all observed at very similar frequencies, at 12.6, 60.6, 83.1 and 119.9 cm^{-1}, respectively. There is also a mode in the spectrum at 46.5 cm^{-1}, which was at first naively ascribed to the transition from the first excited crystal field level (13 cm^{-1}) to the second excited crystal field level (60 cm^{-1}), since it corresponds almost exactly to their energy difference (47 cm^{-1}). This is impossible however, since this first excited state would have only a negligible population at the measuring temperature (2.5 K, while 13 cm^{-1} corresponds to ~18.7 K). Two more modes are observed, one at very low wavenumber, 7.7 cm^{-1} and one at 135.7 cm^{-1}. The nature of these excitations has is at this moment not been confirmed.

One possibility is that there are two inequivalent Tb^{3+}-sites in the structure below the transition. Consequently, the two different Tb^{3+}-sites are subjected to two (slightly) different kinds of crystal field surroundings, creating a (slightly) different crystal field scheme for the two inequivalent sites. This would be in agreement with the apparent symmetry change at the transition temperature. In this picture, one Tb^{3+}-site would have a crystal field level scheme as predicted by crystal field calculations (black levels in fig. 32) while the crystal field levels of the other Tb^{3+}-site would be given by the modes in fig. 33 which are unaccounted for (green dashed levels in fig. 31). In that case, only one 'green' level is not observed in fig. 33, which could be explained by the fact that it is unresolved against the 'black' 83 cm^{-1} mode. However, the 7.7 cm^{-1} mode could also be the low-lying magnetic excitation that is expected for a spin liquid like $Tb_2Ti_2O_7$. Also, neutron scattering studies[63,64] showed the 12.6 cm^{-1} excitation exhibits a dispersion with a minimum at finite wavevector, very similar to the roton minimum observed in the single-particle excitation spectrum of superfluid ^4He.

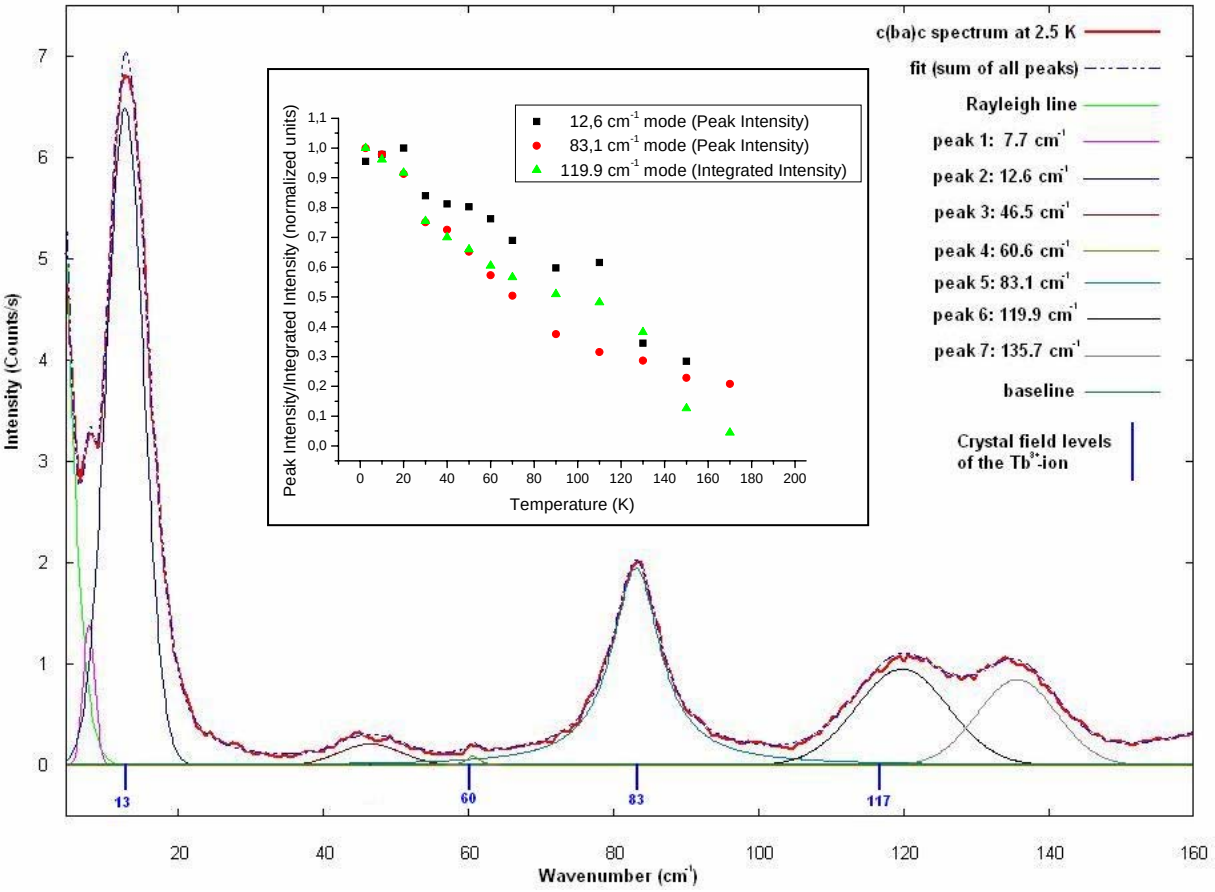

Fig. 33: *The c(ba)c Raman spectrum of $Tb_2Ti_2O_7$ at 2.5 K. The red curve is the measured spectrum, the blue dotted line is the fit to the spectrum. The fit is the sum of all the individual peaks, indicated by the other lines. The calculated crystal field levels (see fig. 32) are indicated by the blue markers along the x-axis. The inset shows the temperature dependence of the amplitudes of the 12.6, 83.1 and 119.9 cm^{-1} peaks. For easy comparison, these amplitudes have been normalized to the 2.5 K amplitudes. This plot shows clearly that they disappear at the temperature of the bump/kink feature in the magnetic susceptibility (fig. 20).*

The inset of fig. 33 shows the temperature dependence of the peak intensities of the 12.6, 83.1 modes and the integrated peak intensity of the 119.9 cm^{-1} mode. For the 12.6 and 83.1 cm^{-1} modes the peak intensities of the modes are depicted, since this gives a more realistic impression of the temperature dependence of the modes (while fitting these modes, their width (and thus integrated intensity) diverges at higher temperatures to account for background signals). The data points have been normalized to their 2.5 K values for easy comparison. From all three curves it is quite clear these crystal field excitations disappear at the same temperature, around 180-185 K, about the temperature where also the bump/kink feature in the magnetic susceptibility of $Tb_2Ti_2O_7$ is observed (see fig. 20). Since its intensity is an order of magnitude smaller, the 60.6 cm^{-1} mode is much harder to fit. Therefore it was not possible to determine the temperature dependence of this mode. The fact that the crystal field modes appear simultaneously at the same temperature when cooling shows that their appearance is very likely due to a symmetry change in the $Tb_2Ti_2O_7$ structure, rather than to thermal depopulation of the levels. This, in turn, forms the third and strongest indication that the $Tb_2Ti_2O_7$ system undergoes a phase transition around the temperature 180-185 K.

C.3.2.) Raman spectroscopy of gadolinium titanate ($Gd_2Ti_2O_7$)

In order to confirm the existence of a phase transition in the rare earth titanates and to definitively establish the nature of the low-lying modes in $Tb_2Ti_2O_7$, the compound $Gd_2Ti_2O_7$ was subjected to a Raman investigation in very much the same way as $Tb_2Ti_2O_7$. What is expected from the comparison between the temperature dependencies of the $Tb_2Ti_2O_7$ and $Gd_2Ti_2O_7$ Raman spectra is firstly, to be able to confirm the phase transition in the rare earth titanates.
Secondly, since the Gd^{3+}-ion in $Gd_2Ti_2O_7$ has no low-lying crystal field excitations, which the Tb^{3+}-ion in $Tb_2Ti_2O_7$ does have, it should be possible to distinguish the crystal field excitations that appear below the phase transition from the other modes appearing due to the phase transition.

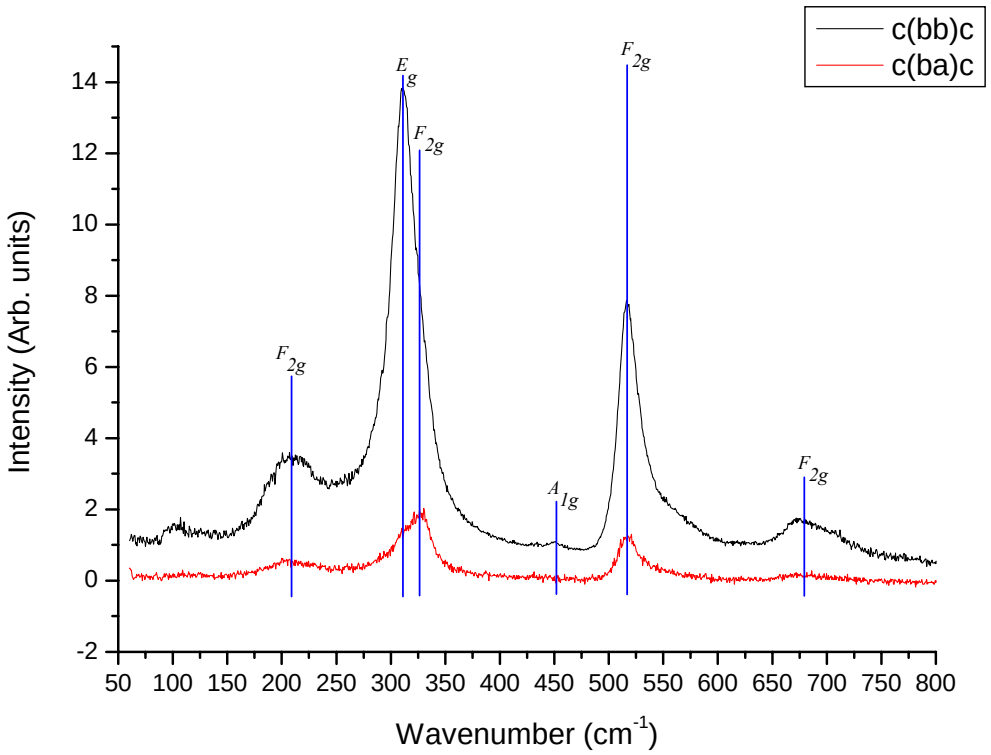

Fig. 34: *Room temperature Raman spectra of $Gd_2Ti_2O_7$ in both c(bb)c and c(ba)c configuration. Also, the assignment of the irreducible representations of the Raman active modes to the observed peaks is indicated. The spectra are very similar to the $Tb_2Ti_2O_7$ spectra of fig. 26.*

For this purpose, the polished sample slice of $Gd_2Ti_2O_7$ was mounted in the flow cryostat in the same way the $Tb_2Ti_2O_7$ sample was mounted. The sample was pumped to a vacuum pressure of ~10^{-7} bar. Once this pressure was reached, the room temperature (295 K) c(bb)c and c(ba)c Raman spectra of $Gd_2Ti_2O_7$ were measured (fig. 34). $Gd_2Ti_2O_7$ and $Tb_2Ti_2O_7$ have the same space group (*Fd-3m)* and occupied sites so, as in the case of $Tb_2Ti_2O_7$, group theory expects the A_{1g}, E_g and $4F_{2g}$ as the Raman active modes for $Gd_2Ti_2O_7$ (the $8F_{1u}$ modes are infrared active and the remaining modes are optically inactive). The assignment of the irreducible representations of the Raman active modes to the observed peaks in the room

temperature Raman spectra of $Gd_2Ti_2O_7$ is depicted in fig. 34. This assignment is based on comparison with assignments in other works[61,61,61], on the assignment in $Tb_2Ti_2O_7$ and on measurements of the angular dependence of the peak intensities (where the angle between the incoming light polarization and the b-axis was varied from -45° to 45°). Comparison between the room temperature Raman spectra of $Gd_2Ti_2O_7$ (fig. 34) and $Tb_2Ti_2O_7$ (fig. 26) yields the conclusion that the nature of the R^{3+}-ion has only slight influence on the Raman spectra at this temperature. This is also expected from group theory, since the R^{3+} (16(d)) sublattice does not have Raman active irreducible representations ($A_{2u} + E_u + 2F_{1u} + F_{2u}$).

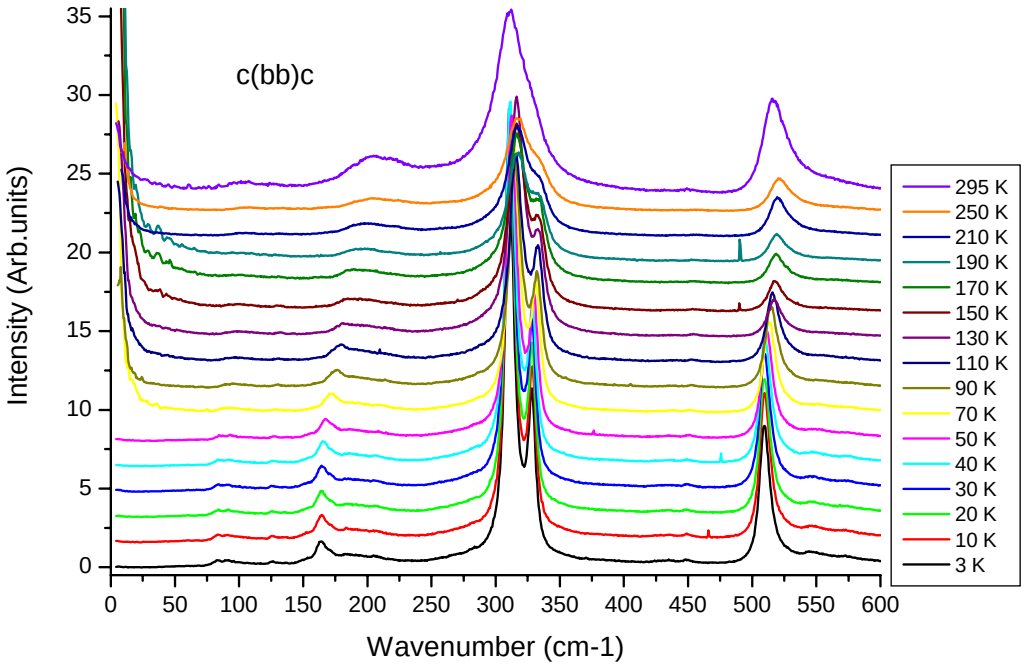

Fig. 35: *Temperature dependence of the c(bb)c Raman spectrum of $Gd_2Ti_2O_7$. The spectrum shows several changes between the temperatures 170 K and 150 K..*

As was done for $Tb_2Ti_2O_7$, the full temperature dependence of both the c(bb)c and the c(ba)c spectrum was measured next. This was done by subsequently bringing the sample into thermal equilibrium with the cooling helium flow at the desired measuring temperatures (ranging from 295 to 3 K). Fig. 35 shows the full temperature dependence of the c(bb)c spectrum of $Gd_2Ti_2O_7$.

The temperature dependence of the c(bb)c spectrum of $Gd_2Ti_2O_7$ is very similar to that of $Tb_2Ti_2O_7$ (fig. 28). Also here, there are several changes when comparing the spectra in going down in temperature. There is the shape change/frequency shift of the ~206 cm^{-1} F_{2g} mode, the frequency shifts and sharpening of the ~313 cm^{-1} E_g and the ~ 330 cm^{-1} F_{2g} modes (making them more distinguishable), the frequency shift and sharpening of the ~515 cm^{-1} F_{2g} mode and the appearance of some new modes around ~83, ~91, ~165, ~545 and ~575 cm^{-1}. All of these changes are also observed in the temperature dependence of the $Tb_2Ti_2O_7$ c(bb)c spectrum, albeit at slightly different frequencies. The other mayor difference is the fact that the ~310 and ~330 modes in fig. 35 are much sharper than in the corresponding modes in $Tb_2Ti_2O_7$ (fig. 28).

The temperature dependence of the c(ba)c spectrum of $Gd_2Ti_2O_7$ is depicted in fig. 36. As in the $Gd_2Ti_2O_7$ c(bb)c spectrum, several changes are observed when going down in temperature. The shape change/frequency shift of the ~206 cm^{-1} F_{2g} mode, the frequency shifts of the ~313 cm^{-1} E_g and the ~ 330 cm^{-1} F_{2g} modes (which make them more distinguishable) the frequency shift and sharpening of the ~515 cm^{-1} F_{2g} mode and the appearance of some new modes around ~83, ~87, ~165, ~545 and ~575 cm^{-1} are also observed in the c(ba)c spectrum.

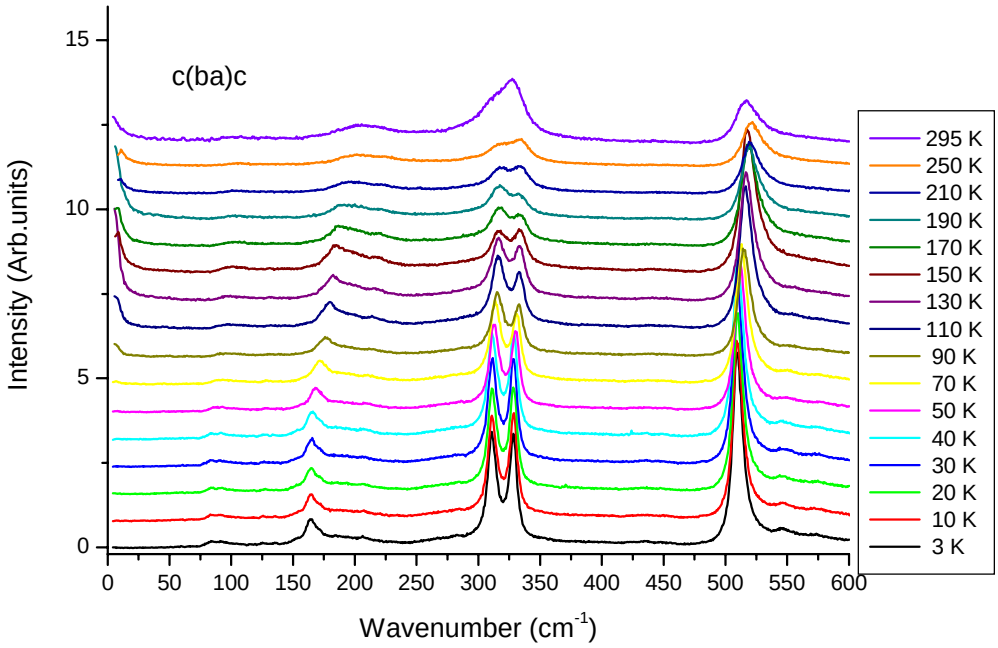

Fig. 36: *Temperature dependence of the c(ba)c Raman spectrum of $Gd_2Ti_2O_7$. The spectrum shows several changes when going down in temperature, all of which are also seen in the very temperature dependence of the $Tb_2Ti_2O_7$ c(ba)c Raman spectrum (fig. 31).*

When comparing fig. 36 to its $Tb_2Ti_2O_7$-analogue (fig. 31), it is immediately confirmed which modes are Tb^{3+} crystal field levels in fig. 31, since these modes are absent in $Gd_2Ti_2O_7$. For easy comparison, the room and low temperature modes ascribed to phonon excitations in the c(bb)c and c(ba)c spectra of both $Tb_2Ti_2O_7$ and $Gd_2Ti_2O_7$ are tabulated in table 3 (new modes in the low temperature spectrum are indicated in blue), as well as the crystal field excitations observed in the Raman spectra of $Tb_2Ti_2O_7$.

Yet another indication pointing towards the existence of a phase transition in the $R_2Ti_2O_7$ family is the fact that at low temperature, in both $Tb_2Ti_2O_7$ and $Gd_2Ti_2O_7$ there are more than 6 Raman active phonons observed (the maximum number Raman active modes for a system of space group Fd-3m is 6), which means the symmetry of the system at low temperature is lower than Fd-3m.

Table 3	**$Tb_2Ti_2O_7$**		**$Gd_2Ti_2O_7$**	
Spectrum:	c(bb)c	c(ba)c	c(bb)c	c(ba)c
Room temperature phonon modes	205, 304, 317, 449, 515, 687	205, 304, 317, 515, 687	206, 313, 330, 451, 515, 681	206, 313, 330, 515, 681
Low temperature (3K) phonon modes	83, 90, 170, 190, 295, 325, 449, 511, 555, 580	170, 190, 295, 325, 511, 555, 580	83, 91, 165, 193, 311, 328, 448, 515, 545, 575	83, 91, 165, 193, 311, 328, 515, 545, 575
Low temperature crystal field excitations	Only very weak (leakage) signals of modes observed in the c(ba)c spectrum	7.7, 12.6, 46.5, 83.1, 119.9, 135.6	-	-

All mode frequencies are in (cm^{-1}) (the highest wavenumber mode (~685 cm^{-1}) is not included with the low temperature modes since this range was not measured at 3 K for both Tb $Tb_2Ti_2O_7$ and $Gd_2Ti_2O_7$)

Thus, it can definitively be concluded that the 12.6, 83.1 and 119.9 cm^{-1} modes observed in the c(ba)c Raman spectrum of $Tb_2Ti_2O_7$ at low temperature are indeed crystal field excitations. Also, this indicates the 7.7, 46,5 and 135.6 cm^{-1} modes in that $Tb_2Ti_2O_7$ c(ba)c Raman spectrum are likely to be Tb^{3+}-ion crystal field excitations, since they are only present in the Tb-variant. With this in mind, combined with the fact that for both $Tb_2Ti_2O_7$ and $Gd_2Ti_2O_7$ the Raman spectra show significant changes going down in temperatures (see table 3), it can also be concluded that $Tb_2Ti_2O_7$ and $Gd_2Ti_2O_7$ (and likely also $Ho_2Ti_2O_7$ and $Dy_2Ti_2O_7$, based on the very similar magnetic susceptibility data) undergo a phase transition around ~175 K. This is quite a surprising find, since these rare earth titanates were believed to show no structural phase transition down to very low temperatures[65]. For the 7.7 cm^{-1}, 46,5 cm^{-1} and 135.7 cm^{-1} modes in the same $Tb_2Ti_2O_7$ c(ba)c Raman spectrum, the evidence is less convincing, since no crystal field levels are expected at these values, nor are there energy differences between the confirmed crystal field levels corresponding to all these energies. The preliminary assignment is thus that these both modes are crystal field levels of a second Tb^{3+}-site, although there is also the possibility that the 7.7 cm^{-1} mode is in fact the excitation of a dispersionless soft mode, which are expected for a spin liquid like $Tb_2Ti_2O_7$. Since $Gd_2Ti_2O_7$ has different ground state than $Tb_2Ti_2O_7$ (it partially orders, albeit at ~1K), such a soft mode would not necessarily exist there. So, the possible observation of this soft mode in $Tb_2Ti_2O_7$ at 7.7 cm^{-1} is not specifically excluded.

D.) Conclusions & Future prospects

The main aim of this master-thesis project was to go through a full research-cycle during the final master year, where every aspect involved in a full research cycle would be addressed. The project was started through a literature study in the subject, geometrically frustrated systems. Taking into account experimental and scientific interest and feasibility of single crystal growth, seven different geometrically systems were chosen to be investigated. The next step was the material synthesis. Using the floating zone technique, several single crystals of $Tb_2Ti_2O_7$, $Gd_2Ti_2O_7$, $Ho_2Ti_2O_7$, $Dy_2Ti_2O_7$ and $CuFeO_2$ were grown at the 'Laboratoire de Physico-Chimie de l'Etat Solide' (LPCES) of the Université Paris-Sud XI. The attempted single crystal growth of two other frustrated systems, $Y_2Mo_2O_7$ and $ZnCr_2O_4$, was unsuccessful. For different reasons, single crystal growth of these compounds using the floating zone technique is not (yet) possible. The single crystals of the rare earth titanates family ($R_2Ti_2O_7$, where R = Gd, Tb, Ho, Dy) that were grown were subsequently characterized by magnetic susceptibility measurements, which revealed similar bump/kink features at approximately the same temperatures, around 170 K. Next, two single crystals, of the $Tb_2Ti_2O_7$ and $Gd_2Ti_2O_7$, were oriented using Laue X-ray Diffraction and subsequently cut and polished into sample slices, appropriate for a Raman investigation. The Raman investigation of these compounds confirmed that indeed, as hinted to by the magnetic susceptibility data, a phase transition occurs in $Tb_2Ti_2O_7$ and $Gd_2Ti_2O_7$ (most probably also in $Ho_2Ti_2O_7$ and $Dy_2Ti_2O_7$) around the temperature of 170 K. This is quite a surprising find, since these rare earth titanates were believed to show no structural phase transition down to low temperatures. The fact that these compounds undergo a phase transition at such a high temperature might completely change the idea of geometrical frustration in these systems. On the other hand, they do show all the general characteristics of geometrically frustrated systems (such as failure to order down to low temperatures), which is not expected for a non-frustrated system. It is thus likely the phase transition corresponds to only a small structural change of one or more the non-magnetic species in the lattice, leaving the frustrated, magnetic lattice intact. In the Raman spectrum of $Tb_2Ti_2O_7$ also some low-lying excitations are observed, most of which can be conclusively assigned to Tb^{3+}-ion crystal field levels, confirming the validity of crystal field calculations. Two other modes are also assigned to Tb^{3+}-ion crystal field levels, although these are not in agreement with the calculations. One of these modes, at very low wavenumber of 7.7 cm^{-1} might even be one of the dispersionless soft modes that are expected for a spin liquid like $Tb_2Ti_2O_7$.

As expected at the beginning of the project, which was not designed to be limited to a single year of research, the research on these geometrically frustrated systems is far from complete. Due to time constraints, only the $Tb_2Ti_2O_7$ and $Gd_2Ti_2O_7$ samples were investigated using Raman spectroscopy. This yielded knowledge about the phase transition in the rare earth titanates. However, it would be interesting to extend this project by conducting a Raman investigation of the $Dy_2Ti_2O_7$ and $Ho_2Ti_2O_7$ samples(both compounds have low-lying crystal field levels), to confirm the existence of a phase transition therein. Additional experiments on the rare earth titanates to determine the nature of the phase transition and its consequence for the magnetic lattice are also desired, as well as experiments investigating the two $Tb_2Ti_2O_7$ Raman modes unaccounted for by crystal field calculations. One possibility would be to grow single crystals of the non-magnetic analogue of the rare earth titanates $Y_2Ti_2O_7$, to investigate whether the phase transition has a magnetic nature, or is due to an instability of the structural 'template'. Despite the project not being fully conclusive, which is was never meant to be, the main goal of the project, going through a full research cycle, was achieved.

E.) Acknowledgements

I would like to thank Prof. Dr. Ir. P.H.M van Loosdrecht for giving me the opportunity to conduct my master-thesis project in the Optical Condensed Matter Physics group of the Rijks*universiteit* Groningen under his supervision and for providing the necessary contacts with the research group in France. I would also like D. Fausti and F. van der Horst for supervision and guidance, M. Mostovoi and D. Khomskii for useful discussions and A. Kamp for technical support. Finally, I would especially like to thank Prof. Alexandre Revcolevschi for letting me conduct my crystal growth experiments in his solid state research group at the Laboratoire de Physico-Chimie de l'Etat Solide' (LPCES) of the Université Paris-Sud XI. Gratitude also goes out to E. Bourdon and G. Dhalenne of the LPCES for, respectively, arranging housing and excellent experimental guidance during my stay in France.

---

[1] Ramirez, A.P., Magnetic systems with competing interactions. *Annu. Rev, Mater. Sci.* **24**, 453 (1994), edited by H.T. Diep (World Scientific, Singapore, 1994)
[2] Schiffer, P. & Ramirez, A.P. Recent experimental progress in the study of geometrical magnetic frustration . *Comments Condens. Matter. Phys.* **18**, 21 (1996-1998)
[3] Villain, J. Insulating spin glasses. *Z. Phys. B* **33**, 31 (1979)
[4] Reimers, J.N., Berlinsky, A.J. & Shi, A.-C. Mean-field approach to magnetic ordering in highly frustrated pyrochlores. *Phys Rev B.* **43**, 865 (1991)
[5] Moessner, R. & Chalker, J.T. Properties of a classical spin liquid: the Heisenberg pyrochlore antiferromagnet. *Phys. Rev. Lett.* **80**, 2929 (1998)
[6] Reimers, J.N. Absence of long-range order in a three-dimensional geometrically frustrated antiferromagnet. *Phys. Rev. B.* **45**, 7287 (1992)
[7] Canals, B. & Lacroix, C. Pyrochlore antiferromagnet: a three-dimensional quantum spin liquid. *Phys. Rev. Lett.* **80**, 2933 (1998)
[8] Gardner, J.S. *et al.* Cooperative paramagnetism in the geometrically frustrated pyrochlore antiferromagnet $Tb_2Ti_2O_7$. *Phys. Rev. Lett*. **82**, 1012 (1999)
[9] Gardner, J.S. *et al.* Dynamic frustrated magnetism in $Tb_2Ti_2O_7$ at 50 mK. *Phys. Rev. B.* **68**, 180401 (2003)
[10] Gingras, M.J.P, *et al.* Thermodynamic and single-ion properties of Tb^{3+} within the collective paramagnetic spin-liquid state of the frustrated pyrochlore antiferromagnet $Tb_2Ti_2O_7$. *Phys. Rev. B.* **62**, 6496 (2000)
[11] Enjalran, M. & Gingras, M.J.P. Theory of paramagnetic scattering in highly frustrated magnets with long-range dipole-dipole interactions: The case of the $Tb_2Ti_2O_7$ pyrochlore antiferromagnet. *Phys. Rev. B.* **70**, 174426 (2004)
[12] Enjalran, M. *et al.* The spin liquid state of the $Tb_2Ti_2O_7$ pyrochlore antiferromagnet: a puzzling state of affairs. *J. Phys.: Condens. Matter* **16**, S673 (2004)
[13] Champion, J.D.M. *et al.* Order in the Heisenberg pyrochlore: The magnetic structure of $Gd_2Ti_2O_7$. *Phys. Rev. B.* **64**, 140407 (2001)
[14] Raju, N.P. *et al.* Transition to long-range magnetic order in the frustrated insulating pyrochlore antiferromagnet $Gd_2Ti_2O_7$. *Phys. Rev. B*. **59**, 14489 (1999)
[15] Stewart, J.R. *et al.* Phase transitions, partial disorder and multi-*k* structures in $Gd_2Ti_2O_7$. *J. Phys.: Condens. Matter* **16**, L321 (2004)
[16] Ramirez, A.P. *et al.* Multiple field-induced phase transitions in the geometrically frustrated dipolar magnet: $Gd_2Ti_2O_7$. *Phys. Rev. Lett.* **89**, 067202 (2002)
[17] Petrenko, O.A. *et al.* Magnetic phase diagram of the antiferromagnetic pyrochlore $Gd_2Ti_2O_7$. *Phys. Rev. B.* **70**, 012402 (2004)
[18] Palmer, S.E. & Chalker, J.T. Order induced by dipolar interactions in a geometrically frustrated antiferromagnet. *Phys. Rev. B.* **62**, 488 (2000)
[19] Santamaria, C. & Diep, H.T. Evidence of partial disorder in a frustrated Heisenberg spin system. *J. Appl. Phys.* **81**, 5276 (1997)
[20] Harris, M.J. *et al.* Geometrical frustration in the ferromagnetic pyrochlore $Ho_2Ti_2O_7$. *Phys. Rev. Lett.* **79**, 2554 (1997)
[21] Rosenkranz, S. *et al.* Crystal-field interaction in the pyrochlore magnet $Ho_2Ti_2O_7$. *J. Appl. Phys.* **87**, 5914 (2000)
[22] Bramwell, S.T. & Harris, M.J. Frustration in Ising-type spin models on the pyrochlore lattice. *J. Phys.: Condens. Matter* **10**, L215 (1998)
[23] Melko, R.G. & Gingras, M.J.P. Monte Carlo studies of the dipolar spin model. *J. Phys.: Condens. Matter* **16**,

R1277 (2004)
[24] Pauling, L. The structure and entropy of ice and of other crystals with some randomness of atomic arrangement. *J. Am. Chem. Soc* .**57**, 2680 (1935)
[25] Anderson, P.W. Ordering and antiferromagnetism in ferrites. *Phys. Rev.* **102**, 1008 (1956)
[26] Bramwell, S.T. & Gingras M.J.P. Spin ice state in frustrated magnetic pyrochlore materials. *Science* **294**, 1495 (2001)
[27] Ramirez, A.P. *et al.* Zero-point entropy in 'spin ice'. *Nature* **399**, 333 (1999)
[28] den Hertog, B.C. & Gingras, M.J.P. Dipolar interactions and origin of spin ice in Ising pyrochlore magnets. *Phys. Rev. Lett.* **84**, 3430 (2000)
[29] Siddharthan, R. *et al*. Ising pyrochlore magnets: low-temperature properties, 'ice rules', and beyond. *Phys. Rev. Lett.* **83**, 1854 (1999)
[30] Siddharthan, R. *et al*. Spin ordering and partial ordering in holmium titanate and related systems. *Phys. Rev.B* **63**, 184412 (2001)
[31] Bramwell, S.T. *et al.* Spin correlations in $Ho_2Ti_2O_7$: a dipolar spin ice system. *Phys. Rev. Lett.* **87**, 047205 (2001)
[32] Petrenko, O.A., Lees, M.R. & Balakrishnan, G. Magnetization process in the spin-ice compound $Ho_2Ti_2O_7$. *Phys. Rev. B.* **68**, 012406 (2003)
[33] Lundgren, L. *et al.* Dynamics of the relaxation-time spectrum in a Cu-Mn spin-glass. *Phys. Rev. Lett.* **51**, 911 (1983)
[34] Bouchaud, J.-P., *et al.* Separation of time and length scales in spin glasses: temperature as a microscope. *Phys. Rev. B.* **65**, 024439 (2002)
[35] Gardner, J.S., *et al*. Spin dynamics in geometrically frustrated antiferromagnetic pyrochlores. *J. Phys.: Condens. Matter* **16**, S643 (2004)
[36] Reimers, J.N., Greedan, J.E. & Sato, M. The crystal structure or the spin-glass pyrochlore, $Y_2Mo_2O_7$. *J. Solid State Chem.* **72**, 390 (1988)
[37] Gingras, M.J.P. *et al.* Static critical behavior of the spin-freezing transition in the geometrically frustrated pyrochlore antiferromagnet $Y_2Mo_2O_7$. *Phys. Rev. Lett.* **78**, 947 (1997)
[38] Dunsiger, S.R. *et al.* Muon spin relaxation investigation of the spin dynamics of geometrically frustrated antiferromagnets $Y_2Mo_2O_7$ and $Tb_2Mo_2O_7$. *Phys. Rev. B.* **54**, 9019 (1996)
[39] Gardner, J.S. *et al.* Glassy statics and dynamics in the chemically ordered pyrochlore antiferromagnet $Y_2Mo_2O_7$. *Phys. Rev. Lett.* **83**, 211 (1999)
[40] Booth, C.H. *et al.* Local lattice disorder in the geometrically frustrated spin-glass pyrochlore $Y_2Mo_2O_7$. *Phys. Rev. B.* **62**, R755 (2000)
[41] Keren, A. & Gardner, J.S. Frustration driven lattice distortion: An NMR investigation of $Y_2Mo_2O_7$. *Phys. Rev. Lett.* **87**, 177201 (2001)
[42] Bellier-Castella, L. *et al.* Frustrated order by disorder: The pyrochlore anti-ferromagnet with bond disorder. *Can. J. Phys.* **79**, 1365 (2001)
[43] Hagemann, I.S. *et al.* Geometric frustration in $Ba_2Sn_2Ga_3ZnCr_7O_{22}$: a two-dimensional spinel based Kagomé lattice. *Phys. Rev. Lett.* **86**, 894 (2001)
[44] Lee, S.-H. *et al.* Local spin resonance and spin-Peierls-like phase transition in a geometrically frustrated antiferromagnet. *Phys. Rev. Lett.* **84**, 3718 (2000)
[45] Sushkov, A.B. *et al.* Probing spin correlations with phonons in the strongly frustrated magnet $ZnCr_2O_4$. *Phys. Rev. Lett.* **94**, 137202 (2005)
[46] Tchernyshyov, O., Moessner, R. & Sondhi, S.L. Order by distortion and string modes in pyrochlore antiferromagnets. *Phys. Rev. Lett.* **88**, 067203 (2002)
[47] Yamashita, Y. & Ueda, K. Spin-driven Jahn-Teller Distortion in a pyrochlore system. *Phys. Rev. Lett.* **85**, 4960 (2000)
[48] Lee, S.-H. *et al.* Emergent excitations in a geometrically frustrated magnet. *Nature* **418**, 856 (2002)
[49] Uhrmacher, M. *et al.* Perturbed angular correlation measurements in 2D spin-frustrated $CuFeO_2$. *Phys. Rev. Lett.* **76**, 4829 (1996)
[50] Mekata, M. *et al.* Magnetic ordering in delafossite $CuFeO_2$. *J. Magn. Magn. Mater.* **104-107**, 823 (1992)
[51] Fazekas, P. & Anderson, P.W. On the ground state properties of the anisotropic triangular antiferromagnet. *Philos. Mag.* **30**, 423 (1974)
[52] Doumerc, J.-P. *et al.* On magnetic properties of some oxides with delafossite-type structure. *Mater. Res. Bull.* **21**, 745 (1986)
[53] Xu, W.M., Pasternak, M.P. & Taylor, R.D. Pressure-induced onset of long-range magnetic order in two-dimensional spin-frustrated $CuFeO_2$. *Phys. Rev. B.* **69**, 052401 (2004)
[54] Terada, N. *et al.* Anomalous magnetic excitation on triangular lattice antiferromagnet $CuFeO_2$. *J. Magn. Magn. Mater.* **272-276**, e997 (2004)

[55] Kasama, T. *et al.* Partially disordered states of the three-dimensional ANNNI model. *Physica B* **329-333**, 1061 (2003)
[56] Zhao, T.R., Hasegawa, M. & Takei, H. Crystal growth and characterization of cuprous ferrite ($CuFeO_2$). *J. Crystal Growth* **166**, 408 (1996)
[57] Cashion, J. D., Cooke, A.H., Leask, M.J.M., Thorp, T.L. & Wells, M.R. *J. Mater, Sci.* **3**, 402 (1968)
[58] Bramwell, S.T. *et al.* Bulk magnetization of the heavy rare earth titanate pyrochlores – a series of model frustrated magnets. *J. Phys.: Condens. Matter* **12**, 483 (2000)
[59] Mori, M *et al.* Compatibility of $Gd_xTi_2O_7$ pyrochlores ($1.72 \leq x \leq 2.0$) as electrolytes in high-temperature solid oxide fuel cells. *Solid State Ionics* **158**, 79 (2003)
[60] Gupta, H.C. *et al.* Lattice dynamic investigation of the zone center wavenumbers of the cubic $A_2Ti_2O_7$ pyrochlores. *J. Raman Spectros.* **32**, 41 (2001)
[61] Glerup, M., Nielsen, O. F. & Poulsen, F. W. The structural transformation from the pyrochlore structure, $A_2B_2O_7$, to the fluorite structure, AO_2, studied by Raman spectroscopy and defect chemistry modeling. *J. Solid State Chem.* **160**, 25 (2001)
[62] Kuzmany, H. Solid State Spectroscopy – An introduction. *Springer-Verlag Berlin Heidelberg New York,* **ISBN** 3-540-63913-6
[63] Gaulin, B.D. *et al.* Neutron scattering studies of geometrically frustrated pyrochlore antiferromagnets. *Physica B* **241-243**, 511 (1998)
[64] Kanada, M. *et al.* Neutron Inelastic scattering study on a single crystal of $Tb_2Ti_2O_7$, a magnetically frustrated pyrochlore system. *J. Phys. Soc. Japan* **68**, 3802 (1999)
[65] Han, S.-W., Gardner, J.S. & Booth, C.H. Structural properties of the geometrically frustrated pyrochlore $Tb_2Ti_2O_7$. *Phys. Rev. B.* **69**, 024416 (2004)